Theses and Dissertations

Summer 2016

Fiber network and nonlinear models of cell matrix interactions and mechanosensing on fibrous gels

Maziar Aghvami
University of Iowa

Recommended Citation

Aghvami, Maziar. "Fiber network and nonlinear models of cell matrix interactions and mechanosensing on fibrous gels." PhD (Doctor of Philosophy) thesis, University of Iowa, 2016.
https://doi.org/10.17077/etd.ly701oxu

FIBER NETWORK AND NONLINEAR MODELS OF CELL MATRIX

INTERACTIONS AND MECHANOSENSING ON FIBROUS GELS

by

Maziar Aghvami

A thesis submitted in partial fulfillment
of the requirements for the Doctor of Philosophy
degree in Biomedical Engineering in the
Graduate College of
The University of Iowa

August 2016

Thesis Supervisor: Assistant Professor Edward A. Sander

Graduate College
The University of Iowa
Iowa City, Iowa

CERTIFICATE OF APPROVAL

_____

PH.D. THESIS

_____

This is to certify that the Ph.D. thesis of

Maziar Aghvami

has been approved by the Examining Committee for
the thesis requirement for the Doctor of Philosophy degree
in Biomedical Engineering at the August 2016 graduation.

Thesis Committee: _____
Edward A. Sander, Thesis Supervisor

_____
Madhavan L. Raghavan

_____
Nicole M. Grosland

_____
H.S. Udaykumar

_____
Sarah C. Vigmostad

To My Mom, Dad and Sister

ACKNOWLEDGEMENTS

I would like to thank my advisor Dr. Edward A. Sander for his guidance, support and introducing me to this interesting research project. I am also grateful to my committee members and co-authors for their valuable suggestions, and my lab mates for providing a friendly, supportive and fun atmosphere. Last but not least, I would like to extend my deepest gratitude to my family for their continued love, support, encouragement, and immense presence in my everyday life despite being halfway around the world.

ABSTRACT

The formation of organized, functional tissues, and later in life, their limited regeneration in response to injury, or disease, are governed by cell-matrix interactions. Directing and optimizing tissue self-structuring and remodeling in these processes are progressing, but there is still a lack of understanding how these interactions are coordinated across various scales, especially in terms of the role of cell's mechanical environment. This environment is affected by the organization, and the properties of the local extracellular matrix (ECM) in which physical forces are communicated at the cellular and fiber levels. Thus, mechanical cues along with biochemical and electrical cues contribute to a complex process of self-structuring and remodeling that necessitates the development of computational frameworks which can incorporate a large number of experiments into a comprehensive whole.

Theoretical development of the mechanics of ECM substrates has relied on making many simplifying assumptions. Continuum-based models are commonly used for these purposes, but they mostly do not consider the fiber-fiber interactions and non-affine microstructural reorganization of fibrous materials. Another limitation of these models is that they generally do not include autonomous mechanoresponsive cells. These cells generate forces that reorganize the ECM and alter their activity in response to forces from the ECM. The purpose of this work is to develop such a fiber-based computational model and to account for active cellular component to help understand the dynamics and reciprocal nature of the cell's mechanical environment.

PUBLIC ABSTRACT

The formation of organized, functional tissues, and later in life, their limited regeneration in response to injury, or disease, are governed by cell-matrix interactions and cell's mechanical environment.

Theoretical development of the mechanics of extracellular matrix (ECM) substrates has relied on making many simplifying assumptions (i.e., they mostly do not consider the fiber-fiber interactions in fibrous tissues, and do not include the autonomous mechanoresponsive cells, which generate forces that reorganize the ECM and alter their activity in response to forces from the ECM). The purpose of this work is to develop such a fiber-based computational model and to account for active cellular component to help understand the dynamics and reciprocal nature of the cell's mechanical environment.

TABLE OF CONTENTS

LIST OF TABLES

LIST OF FIGURES

cytoskeleton mechanical properties. Neighboring nodes i and j are connected by elastic spring with elasticity coefficient E_{ij} and viscous dashpot with viscosity coefficient μ, in parallel. The active forces F_i are applied at the front of the cell. A representative force is marked by an arrow. The cell center is indicated by C 65

CHAPTER 1

INTRODUCTION

1.1 Motivation

Tissue development, remodeling and repair is profoundly affected and directed by the mechanical microenvironment of cells (1-3). The attributes of this complex environment, which include substrate dimensionality, stiffness, porosity, and topology, are also important to consider in a number of strategies in regenerative medicine, such as in designing the stem cell niche (4, 5). Therefore, a number of experimental and computational studies have been performed to identify the role mechanical environment plays in directing various cell activities, such as cell migration (6), and extracellular matrix (ECM) remodeling (7, 8).

A commonly used experimental technique to study the effect of microenvironment mechanical properties on cell behavior and cell matrix interactions is to culture cells on polyacrylamide (9), PDMS (10), or other synthetic substrates. These substrates are used primarily because they are inexpensive and readily-available biocompatible materials whose mechanical properties are tunable over a range of biologically relevant stiffnesses (9, 11). Another important advantage is that mechanical analysis of the experiments is greatly simplified compared to native tissues due to the linear elastic, homogeneous, and isotropic, properties of these synthetic materials. Although the use of such materials has revealed much about the mechanobiology of various cell types, these materials are limited in that they are not directly comparable to the ECM that these cells reside in. The profile of the material properties of the ECM can

1

be categorized as substantially more complicated (i.e., not linear elastic, heterogeneous, and anisotropic). Much of this character derives from the fibrous nature of the ECM and the fact that these fibers are often connected into networks that organize into hierarchical structures at each scale of the tissue (Figure 1-1). Experiments on fibrous substrates, such as fibrin or collagen, have demonstrated that the cellular response is quite different than for a non-fibrous substrate of comparable bulk stiffness (12-15).
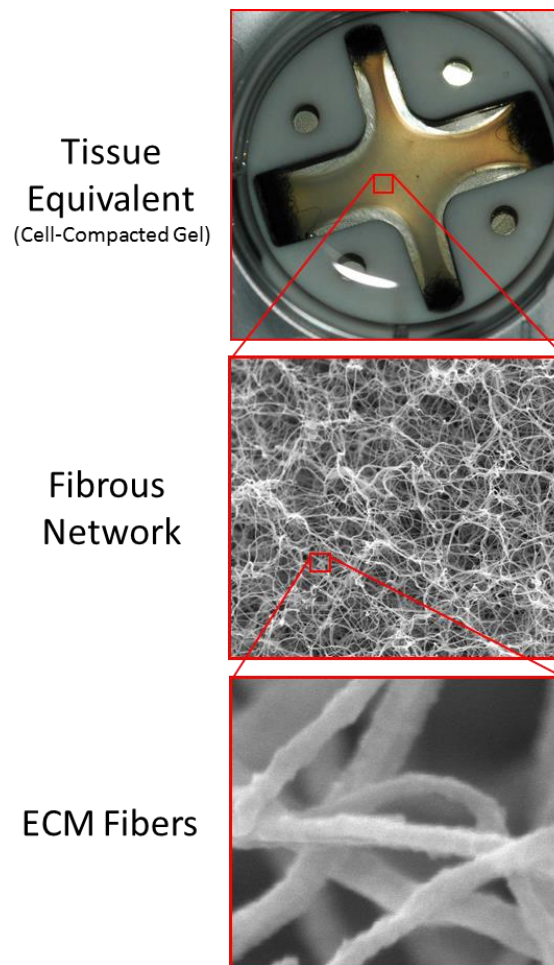
Figure 1-1: Mechanical interactions at the fiber and the cellular levels control tissue development, remodeling, and repair (image courtesy of E.A. Sander).

Several computational models have been developed in order to understand how macroscopic forces affect cell activity (16-19). In these models, the microstructure is often represented as a continuum (17), or they do not properly consider the fibrous nature of the tissue or substrate (16, 18, 19). Furthermore, the cell traction forces on ECM, which can contribute substantially to the overall mechanical responses, may be ignored in such models. It is unclear how cell traction changes force transmission through the gel and how a cell senses its environment, which further limits our ability to engage in tissue engineering and repair. Sen *et al.* (20) modeled a contracting cell placed on a linear elastic substrate, such as PA, and computed the deformations and strain field using finite element analysis. They concluded that the cell can feel on length scales from a few hundred nanometers to a few microns. In contrast to PA gels, it was found experimentally that cells on fibrous gels, such as fibrin and collagen, can sense and deform the gel on much higher length scales (13, 14). Mehrota *et al.* (21) constructed a 2D axisymmetric finite element model of a poly(diallyldimethylammonium chloride) (PDAC)/sulfonated polystyrene, sodium salt (SPS) film to study how the thickness of the substrate influences the mechanosensitive length scale of cells. They assumed a constant cell traction force and a linear elastic material. They found that effective stiffness decreases linearly with substrate thickness, and reaches an asymptotic value around 50 microns. The mechanosensitive length scale of the cell is governed not only by Young's modulus but also by thickness of the substrate.

While most previous work has used synthetic, linear elastic materials, fibrous and nonlinear constitutive properties of biological gels can have a dramatic effect on cell mechanosensing. Notbohm *et al.* (22) developed a nonlinear finite element model for a

3

fiber network representing fibrin gels to simulate localized deformations induced by static cells, and showed that cells in a fibrous matrix induce deformations that propagate over a longer range than predicted by linear elasticity, but the mechanism does not seem to be the proposed microbuckling. Abhilash *et al.* (23) presented a finite element model for 2D discrete fiber networks created with linear elastic fibers, and captured static cell-mediated collagen alignment, deformations, and long-range force transmission. Both models utilized constant displacement boundary conditions for cell traction.

On the other hand, cellular activities are strongly modulated by the mechanical environment (6, 24-28). For example, Lo *et al.* (6) demonstrated that substrate stiffness is an important regulator of cell migration on 2D substrates. Therefore, mathematical models for cell biomechanics and behavior in response to mechanical environment are also needed to resolve these complex relationships and interactions. Agent-based models (ABM) have been applied recently for these purposes (29-31). The rules governing cell behavior can be set up based on physical principles and conservation laws in such models. Dokukina *et al.* (30) constructed a discrete model of fibroblast motility to investigate the mechanics of rigidity sensing by modeling a fibroblast as 2D Delaunay network, with each fiber acting as an elastic spring and a viscous dashpot in parallel connected at nodes. By applying an external force to the front nodes in the lamellipodium, the model was able to reproduce cell preference for stiffer surfaces.

1.2 Objective

Characterizations of the cellular response to the environmental cues, the cell mechanosensing, and the substrate remodeling have been explored, but many of the

4

details require further study, in part because many of these cues present together, evolve reciprocally, and feedback into each other. For example, a cell may exert forces to locally reorganize ECM, the reorganization then changes the local effective stiffness, and the traction forces change (13). The goal of this dissertation is to develop and adapt a fiber-based computational model and to account for active cellular component in order to understand and predict the role of cell matrix interactions and mechanosensing in tissue self-structuring and fiber reorganization. This work involves a characterization of the role of mechanical environment, expands a fiber-based modeling framework, and incorporates autonomous cell-matrix interactions.

CHAPTER 2

THE EFFECT OF CELL COMPACTION ON REMODELING OF COLLAGEN GELS IN A MULTI-SCALE MECHANICAL MODEL

2.1 Introduction

Cell activity is controlled by a complex set of spatially and temporally varying environmental cues. It has been demonstrated that the properties of the surrounding extracellular matrix (ECM) and the local mechanical environment profoundly influence cell behavior (3, 11, 32-34). The mechanical environment is controlled in part by the composition and stiffness of the local ECM and by the manner in which physical forces applied at the tissue-level propagate down to the cellular level. Forces are communicated to the cell through cell-cell and cell-ECM attachments via a number of signaling pathways that result in the conversion of mechanical signals into chemical signals (i.e. mechanotransduction) (35-37).

Changes in mechanical environment have been attributed to pathological remodeling in osteoporosis (38, 39), glaucoma (40, 41), atherosclerosis (42, 43), and aneurysm (44), to cite just a few examples. Physical forces and changes in ECM stiffness have also been implicated in tumor metastasis (45-47). The specifics on how such changes drive pathological tissue remodeling, however, remain poorly understood. Part of the confusion derives from the fact that the local mechanical environment is dynamic and dependent on the integrated and reciprocal response of the entire tissue.

In the field of tissue engineering, deformations applied to cell-seeded scaffolds have also been shown to modulate synthetic and enzymatic cell activity and

6

differentiation (48-51). As a result, engineered tissues are commonly conditioned mechanically by dynamic stretching, which improves mechanical properties beyond the level that can be derived solely from biochemical stimulants. The choice of a particular waveform and magnitude of stretch, however, is largely empirical because the precise relationships between the applied deformations and the cellular response are poorly understood. Furthermore, the amplitude and frequency of the conditioning protocols often does not change over the course of the culture period even though the remodeling process changes the local mechanical environment, ostensibly in an effort to drive it to a point of tensional homeostasis (52). Syedain *et al.* found that fiber-based engineered tissues had improved composition and mechanical properties when the magnitude of cyclic distension was incrementally increased every few days compared to those subjected to a constant magnitude over the duration of the experiment (53). These results suggest that in order to maintain a synthetic response in growing constructs, the mechanical environment must change faster than the cells can adapt to it. Since the relationships between mechanical stimulation and ECM remodeling are complex, interdependent, and dynamic, theoretical remodels are required for understanding the underlying phenomena so that the conditioning process can be optimized to produce functional engineered tissues.

The purpose of this chapter is to lay the foundation for answering the questions: how does cell compaction change the distribution of force, strain and fiber alignment in a collagen gel, and what is the relationship between macroscopic tissue strain and microscopic tissue strain when these constructs are deformed? These are critical questions that must be answered in order to optimize mechanical conditioning procedures designed to produce engineered tissues with mechanical functionality similar to native

7

tissues, particularly as the tissues and cells adapt to the mechanical environment. As an initial exploration into this area, we incorporated the effect of cell tractions on developing isometric tension in the surrounding fibers of fiber-based collagen gels in a multi-scale mechanical model (54).

2.2 Methods

2.2.1 Multi-scale Model

The multi-scale modeling framework employed here was developed previously to examine mechanical coupling between scales in collagen gels (55-57) and other biomaterials (58, 59). The model treats the macroscopic domain of the material with the standard Galerkin finite element method and links it to a description of the microstructure via local microscopic fiber network problems and the theory of volume averaging (60, 61). The essential equations in the model include: (1) a constitutive equation describing the mechanical behavior of a single fiber, (2) an equation that provides the volume-averaged stress of a collection of cross-linked fibers that form a network, (3) and an equation for the balance of macroscopic stress (55, 56). Briefly, macroscopic displacements on the FE mesh are mapped to the boundaries of the microscopic networks, each centered at the eight Gauss points within each element, through the use of tri-linear basis functions. The cross-linked fibers in the networks then reorganize and deform to satisfy force equilibrium. The volume-averaged stress from each network is then incorporated into the macroscopic stress balance, and an iteration is conducted until the positions of the FE nodes and the fiber reorganization combine to produce a state of equilibrium throughout the model. The constitutive equation of a fiber is

8

$$F = \frac{E_f A_f}{B} \left[\exp(B\varepsilon_f) - 1 \right] \tag{2.1}$$

where E_f is the Young's modulus at infinitesimal strain, A_f is the cross-sectional area of a fiber, B is a fitting parameter that controls the nonlinearity of the force response, and ε_f is the Green's strain of the fiber and is calculated as $\varepsilon_f = 0.5(\lambda_f^2 - 1)$, where λ_f is the fiber stretch ratio. In this study, a value of $E_f A_f = 1.4 \times 10^{-8}$ N and a value of $B = 3.8$ were used for both cellular and ECM networks based on our previous work. The volume-averaged Cauchy stress of the fiber network, $\langle \sigma_{ij} \rangle$, is calculated in discrete form as

$$\langle \sigma_{ij} \rangle = \frac{1}{V} \int_V \sigma_{ij} dV = \frac{1}{V} \sum_{boundary\ nodes} x_i F_j \tag{2.2}$$

where V is the volume of the network, σ_{ij} is the local microscopic stress, and x_i and F_j are the position and forces on the boundary nodes, respectively. The macroscopic stress balance is

$$\langle \sigma_{ij,i} \rangle = \frac{1}{V} \oint_{\delta V} \left(\sigma_{ij} - \langle \sigma_{ij} \rangle \right) u_{k,i} n_k dA \tag{2.3}$$

where u is the displacement of the network boundary δV, and n is the unit normal vector to the network surface.

2.2.2 Microscale Networks and Cell Compaction

The collagen gel microstructure was approximated by a collection of 3D fiber networks that have been shown to resemble the structure and heterogeneity observed experimentally (32, 33). In this study, each element in the FE mesh was randomly assigned a 3D fiber network containing on average 323 ± 26 cross-linked fibers. The

9

networks were created so that the fibers were preferentially aligned in the *xy*-plane (90% of the fibers were oriented within 10° of the *xy*-plane). In addition, the networks were created so as to be nearly isotropic ($\alpha = 0.15 \pm 0.07$ defined below) within the *xy*-plane. This configuration was chosen to help facilitate comparisons with experiments, in which information about fiber realignment through the thickness is often not available, and the subsequent analysis, which was conducted on the 2D projections of the 3D microstructures.

Network orientation and strength of alignment were quantified by the length-weighted 2D orientation tensor, Ω, which is given by

$$\Omega = \frac{\sum_{i=1}^{NF} l_i \begin{bmatrix} \cos^2 \theta_i & \cos \theta_i \sin \theta_i \\ \cos \theta_i \sin \theta_i & \sin^2 \theta_i \end{bmatrix}}{\sum_{i=1}^{NF} l_i} \tag{2.4}$$

where θ_i is the angle that fiber i makes with respect to the horizontal axis, l_i is the length of fiber i, and the sum is over all of the fibers in the network, *NF*. The eigenvectors and eigenvalues of this Ω represent the principal directions and magnitudes, respectively, of fiber orientation in the network. The strength of fiber alignment was quantified using an anisotropy index α, given by

$$\alpha = 1 - \omega_1/\omega_2 \tag{2.5}$$

where ω_1 and ω_2 are the eigenvalues of Ω, and $\omega_1 \leq \omega_2$. Under this convention, an isotropic network has an α value of 0, and a completely aligned network has an α value of 1 (62).

As a first step towards representing the physics of gel compaction and the development of internal tension, cell tractions were approximated by partitioning the

10

networks in the model into either ECM (non-contractile) networks or cellular (contractile) networks. Therefore, elements designated as cells (or explants) contain only cellular networks, and elements designated as collagen gel only contain ECM networks. For this initial effort, cellular and ECM networks were assigned the same material properties and structure. The only difference between these types of networks was that during the compaction phase of the simulation, the reference length of fibers in the cellular networks was incrementally reduced, which created tension in surrounding fibers of the ECM networks. This approach to modeling cell compaction is only meant to simulate the effects of cell traction forces on the surrounding ECM. It is not meant to reflect the manner in which a cell actually exerts traction forces on the ECM.

2.2.3 Cell Compaction Case Studies

In many applications that involve entrapping cells in gels, the cells are initially distributed homogeneously throughout the gel (e.g., (63)). The cells then compact the gel and produce a fiber alignment pattern that depends in part on cell traction forces, gel geometry, and gel mechanical constraints. In an effort to understand better the mechanisms involved within a less complex setting, several investigators have studied the development of fiber alignment, or "straps", between clusters of cells, or explants (64-66). The explant system allows easier arrangement of cells into simple geometric patterns and facilitates visualization of the mechanisms underlying cell-driven fiber realignment. Thus, the explant system provides a convenient system for understanding how alignment patterns form.

11

We simulated the development of fiber alignment in an explant system under similar conditions to those of Sawhney and Howard (65). In that study, three mouse fibroblast explants (each consisting of approximately 4,000 cells) were placed in a 1.7 mg/mL collagen gel in a triangular pattern spaced approximately 1 mm apart, and the development of fiber alignment between explants was monitored with time-lapse imaging over an 18 hour period. To represent a typical experiment (Figure 2-1A), a one-element thick square FE mesh consisting of 576 tri-linear hexahedral elements and 1250 nodes was created to represent a spatial scale of 10 mm x 10 mm x 2 mm (length, width, thickness). The FE domain (Figure 2-1B) was then partitioned into three triangularly arranged cellular domains, each consisting of four adjacent elements arranged as a square and containing only cellular networks. These cellular domains represent the explants, and they were embedded within a surrounding collagen gel domain consisting of ECM networks.
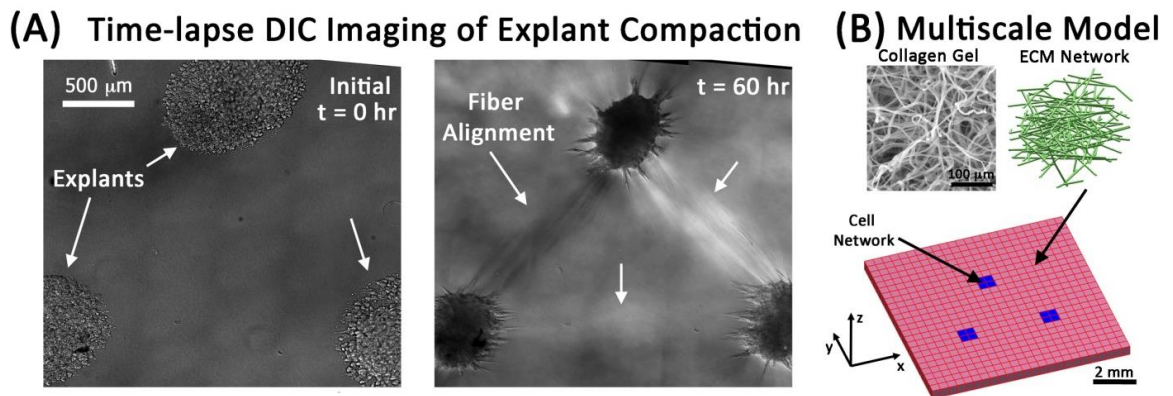
Figure 2-1: "Strap" formation between explants and the multiscale modeling strategy. (A) A triangular explant configuration develops strong fiber alignment between fibroblast explants after 60 hours. Images are montages of sixty 20x DIC images (images from Dr. Sander's lab). (B) Multiscale models consist of cellular networks (blue) that are configured in an analogous manner to the experiments and that contract to 40% of their original length to produce tension and reorganization in the surrounding ECM networks.

Three simulation cases were investigated for 40% cell-driven compaction by three triangularly arranged explants:

- Case 1: four fixed boundaries (top, bottom, left, and right surfaces) during compaction

- Case 2: two fixed boundaries (top and bottom surfaces) during compaction, followed by 50% uniaxial stretch

- Case 3: three symmetry boundaries (bottom, left, and back surfaces) during compaction. For each scenario, unless specified above, the boundary was free.

We also repeated case 1 for 2 explants, 4 explants, and 5 explants to assess the role of explant geometry, and we repeated case 2 for no explants to assess the model mechanics without cell compaction.

To simulate cell compaction, the reference lengths of the fibers in the cellular networks were shortened either 4% (cases 1 & 2) or 2% (case 3) with each step, and the restructuring of fibers in both ECM and cell networks required to achieve mechanical equilibrium was determined iteratively. This process continued until the cellular network fiber reference lengths were 40% shorter than the original fiber lengths (i.e., either 10 or 20 steps). To apply uniaxial stretch (case 2), the top boundary was then displaced 0.5 cm over ten equally spaced steps (0.05 cm/step) while the bottom boundary remained fixed. Fiber stretch ratios were used to calculate the Lagrangian strain for the fibers. Fiber stretch ratios, which were defined relative to the original fiber length, were only calculated for the ECM networks due to difficulties with interpretation for the cellular networks, where the reference lengths were changed with each step to generate tension.

13

Since the FE domain contains 4,608 networks and consists of approximately 1.5 million fibers, the computational demands for these simulations were large. Simulations were run using a custom parallelized C code with message passing interface (MPI) on high performance computing resources. All post processing was done using Matlab.

2.3 Results

The effect of cell compaction on microstructural reorganization, development of internal tension, and altered mechanical behavior in explants embedded in collagen gels was studied in a multi-scale modeling framework for a number of different scenarios. Compaction was achieved by incrementally shrinking the reference length of cellular network fibers until it had been reduced by 40%, which we refer to as 40% compaction, for all simulations.

For case 1, four different explant configurations were simulated. Varying levels of fiber realignment were observed in the surrounding ECM networks for each configuration (Figure 2-2). Fiber realignment increased with the amount of compaction, first in the networks nearest the explants. As the amount of compaction increased, fiber realignment spread outward on paths directed towards the other explants and towards the fixed boundaries. The change in ECM network fiber alignment with respect to the initial configuration ($\Delta\alpha$) also increased with the number of explants. At the end of compaction, $\Delta\alpha$ reached values of 0.037 ± 0.048 (mean $\pm$ standard deviation, two explants), 0.051 ± 0.060 (three explants), 0.067 ± 0.064 (four explants), and 0.072 ± 0.071 (five explants). The $\Delta\alpha$ values are low because they were obtained by averaging over all ECM networks in the model, even though only a fraction of the ECM networks were impacted by cell

14

compaction. As the number of explants increased the fraction of ECM networks with $\Delta\alpha$ > 0.08 increased from approximately 11% to 30%. Within this subset $\Delta\alpha$ values were as high as 0.40 for some ECM networks immediately adjacent to the explants.
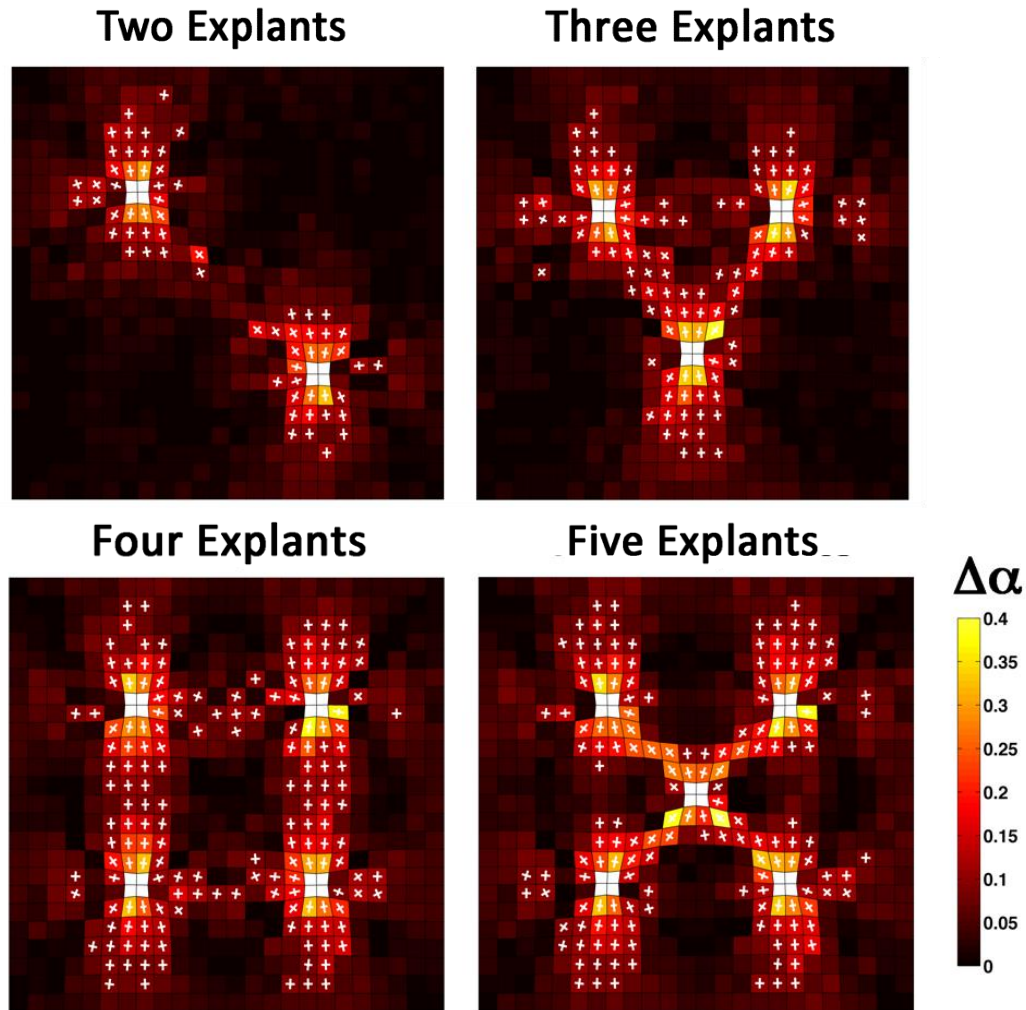
Figure 2-2: Top-view of fiber network realignment after 40% compaction for case 1. ECM networks develop varying patterns of fiber alignment between explants in a configuration dependent manner. The color map indicates the change in the degree of fiber alignment ($\Delta\alpha$) between the initial traction free configuration and 40% compaction. Also depicted are the principal directions of fiber alignment (white crosses). For clarity directions are only shown for those elements with $\Delta\alpha$ > 0.08.

Among the different explant configurations examined above, the triangular configuration (Figure 2-2B) was further explored to determine how boundary conditions

15

affect model predictions of gel restructuring in response to cell compaction. As was observed with fiber realignment, cell compaction produced the largest strains in the networks immediately around and between the explants in a manner that depended on the boundary conditions (Figure 2-3). For the case of four fixed boundaries (Figure 2-3A, D), the direction of maximum principal strain was axially aligned between all three explants. When the left and right boundaries were freed (Figure 2-3B, E), the strain in the 16 elements directly between the bottom two explants decreased from 0.062 ± 0.013 to 0.057 ± 0.019 and the strain pattern between explants switched from a triangular shape to an inverted v shape. In contrast, when symmetry conditions were applied and the surfaces were allowed to freely translate with compaction (Figure 2-3C, F), the direction of maximum principal strain changed and was generally perpendicular to the axis between explants. At the end of 40% compaction, the average maximum principal strains were 0.051 ± 0.024, 0.044 ± 0.026, and 0.035 ± 0.032, for the fixed, uniaxial, and free boundary simulations, respectively.
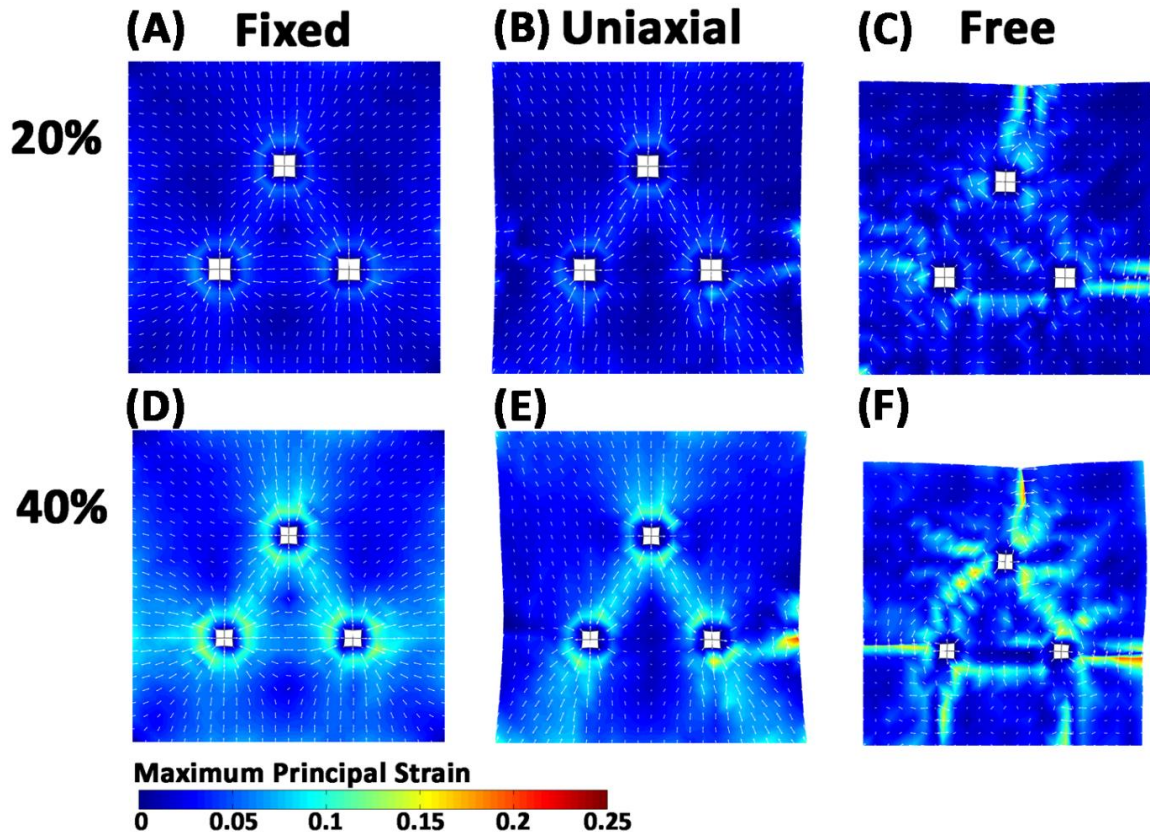
Figure 2-3: Strain developed during 20% and 40% compaction for three explants. (A) top, bottom, left, and right boundaries are fixed, (B) top and bottom are fixed, and (C) symmetry boundary conditions are applied to the left, bottom, and back faces. Maximum principal strain patterns change in accord with the applied boundary conditions. White arrows show principal direction.

The effect of cell compaction on the mechanical response of the model construct was evaluated by comparing the response of the 40% compacted, three-explant model to an equivalent model without cellular networks (i.e. no explants), where both models were subjected to uniaxial extension (Figure 2-4). Prior to stretch, 40% compaction resulted in the development of a small amount of isometric force (8 mN) on the surface perpendicular to the axis of stretch (Figure 2-4A). The force then increased nonlinearly with stretch up to 0.62 N at a macroscopic stretch ratio of $\lambda = 1.5$ (i.e. 50% stretch). The force also increased with stretch in the explant-free model, but the force was always

17

www.manaraa.com

slightly lower (e.g. 0.58 N at $\lambda = 1.5$) than in the three-explant model. The average

principal strain was also lower in the no-explant model (Figure 2-4B) compared to the

three-explant model (Figure 2-4C), reaching values of 0.639±0.048 and 0.649±0.095,

respectively at $\lambda = 1.5$. Regional variations in strain were also more pronounced in the

three-explant model, particularly around the explants, where regions of tension and

compression were observed (Figure 2-4C).
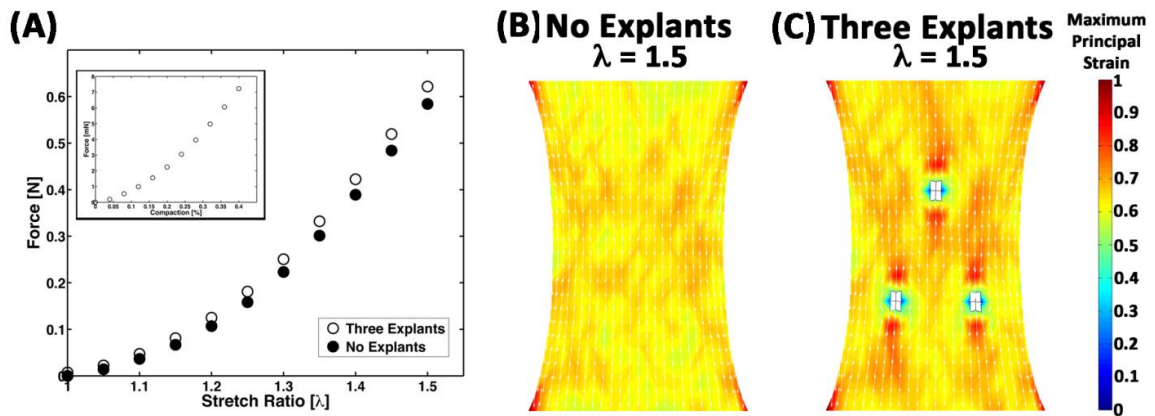
Figure 2-4: Comparison of mechanical response. (A) The force on the boundary during uniaxial extension for the case of 40% compaction for three explants (circles) is higher than the case where all of the networks are ECM networks (i.e. no explants). The inset plot shows the increase in force that develops on the boundary during the compaction process prior to uniaxial extension. (B) Regional differences in strain, particularly around the explants, are apparent at full stretch ($\lambda = 1.5$).

During the compaction phase of the simulations, the average ECM fiber strains

were very small and increased from 0.001 ± 0.013 at 20% compaction (Figure 2-5A) to

0.005 ± 0.021 at 40% compaction (Figure 2-5B). The strains were small because the

majority of fibers in the model were not strongly impacted by explant compaction. At

20% and 40% compaction, the fraction of fibers in the model with tensile strains

exceeding 1% increased from 9.4% to 21.6%, respectively, and the fraction of fibers with

compressive strains in excess of 1% increased from 3.2% to 5.4%, respectively. These

18

fibers were primarily located in elements immediately around the explants and along the axes between explants.

The average fiber strain increased with uniaxial extension from 0.101 ± 0.113 at 25% stretch (Figure 2-5C) to 0.252 ± 0.241 at 50% stretch (Figure 2-5D). By comparison, the average fiber strain in the no-explant model was slightly lower, 0.094 ± 0.103 at 25% stretch and 0.243 ± 0.230 at 50% stretch. The distribution of all fiber strains in the model was also similar in shape to the three-explant model (data not shown).
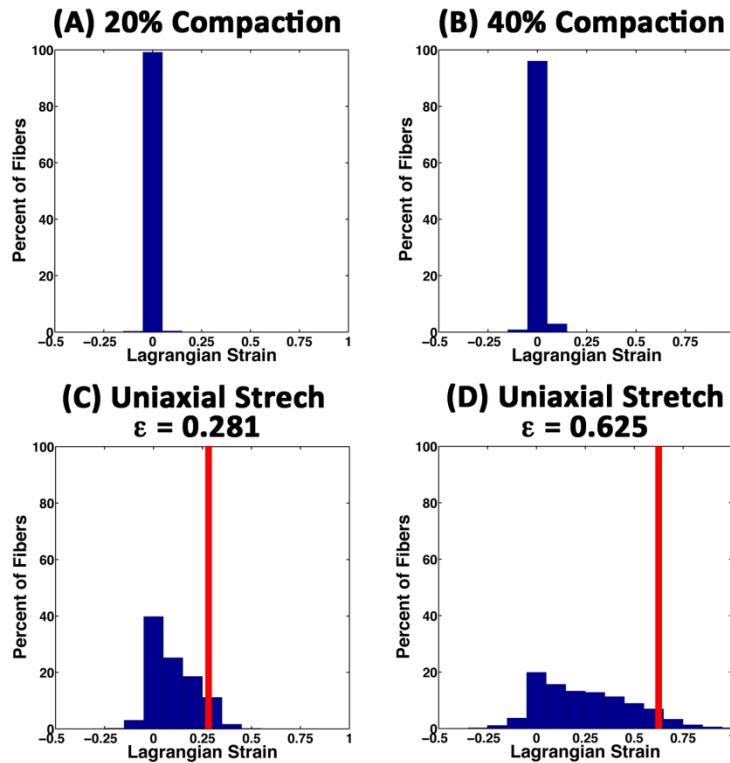
Figure 2-5: Histograms of fiber strain in all ECM networks for uniaxial stretch of the three-explant model. (A,B) During the compaction phase of the simulations a small fraction of fibers developed small tensile and compressive strains. (C,D) With uniaxial stretch a wide range of fiber strains were observed, most of which were below the amount of stretch applied macroscopically (red line). The distribution of fiber strains in the no-explant model (data not shown) were similar in shape to those in C and D.

19
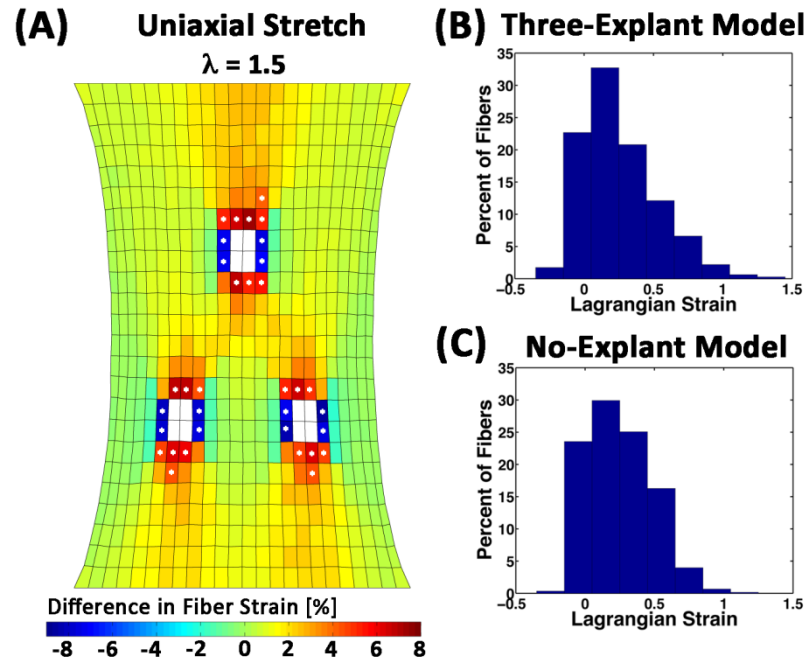
Figure 2-6: Differences in average fiber-level strain at 50% uniaxial stretch. (A) Regional variations in the average fiber-level strain in each element were apparent when the strains in the no-explant model were subtracted from those in the three-explant model. The largest differences were found in the elements around the explants (white). Differences in fiber strain that exceeded ± 4% are highlighted with a star. Histograms of the strains for all 88,728 fibers in the starred elements for the three-explant model (B) and no-explant (model).

Even though the difference in the overall average fiber strain between the models was small, the presence of the compacting explants resulted in regional differences in average fiber strain, particularly near the explants (Figure 2-6A and Figure 2-7A, B). For the three-explant model, average fiber strains were higher in elements above and below the explants, and lower in elements left and right of the explants than in the no-explant model. The starred elements in Figure 2-6A indicate the locations where the difference in strain exceeded 4%. For the red/orange starred elements (22 elements) the average fiber strain was 0.311 ± 0.309 and 0.256 ± 0.229 in the three-explant and no-explant models, respectively. In the blue elements (12 elements) the average fiber strain was $0.170 \pm$

www.manaraa.com

0.149 and 0.246 ± 0.227 in the three-explant and no-explant models, respectively. Histograms of fibers in this subpopulation of the elements revealed differences in the distribution profiles as a result of cell compaction (Figure 2-6B, C). Regardless of the model or the location, the fiber strains tended to be much lower than the applied strain because fibers were able to rotate and realign towards the *y*-direction before stretching (Figure 2-5C, D). A small number of fibers, however, experienced amplified strains, some as high as three times the applied strain. Network kinematics and individual fiber strains for two networks are depicted in Figure 2-7. The first network (Figure 2-7C) is from a region of high strain and fiber alignment. During compaction, the network sheared and aligned diagonally along the axis between explants. This diamond shape was maintained during stretch. The other network (Figure 2-7C) also reorganized during compaction, but it shrank laterally with respect to the axis between the bottom explants. The fibers in this network also experience an increase in strain to accommodate the macroscopic stretch, but the reorganization differs markedly from its response to stretch in the no-explant model.
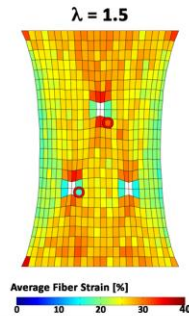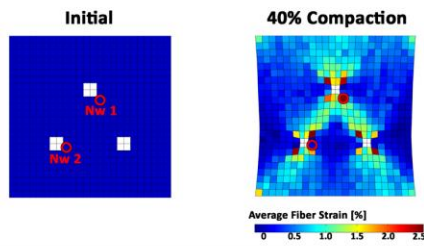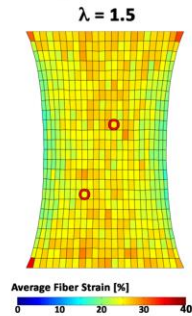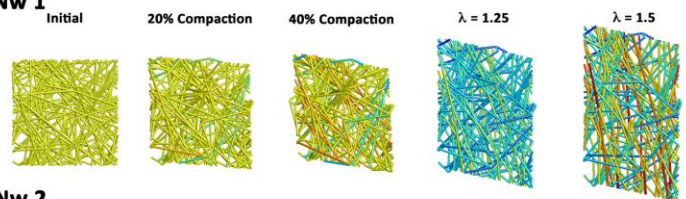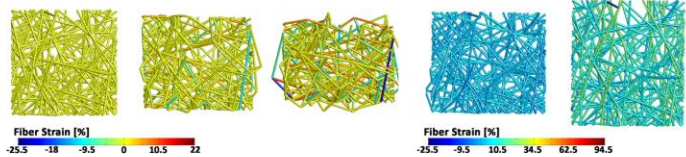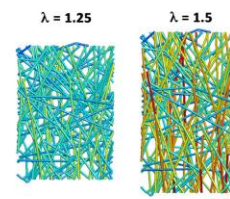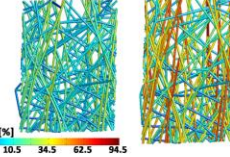
Figure 2-7: Behavior of selected networks. (A,B) Average fiber strains in each element are depicted at select instances for the (A) three-explant model and the (B) no-explant model. The red circles highlight the locations of two networks depicted below. (C) Top-view of network 1, which is associated with an area of high fiber strain. The individual fibers reorganize to satisfy force equilibrium and are color coded to indicate the level of fiber strain. (D) Network 2 is associated with an area low average fiber strain. Prior to uniaxial stretch the network volume shrinks and some fibers are under compression. The fiber strain and kinematics in these networks are compared with those developed in the no-explant model (E,F).

2.4 Discussion

The models examined in this study were inspired by (but did not match exactly) the experiments of Sawhney and Howard (S&H) (65), who reported primarily on the reorganization of collagen fibers between explants in the triangular configuration. For example, the explants in the three-explant model were spaced farther apart (approximately 3.5 mm) than in S&H (approximately 1 mm) (65). There were also

22

differences between the model and the gels in S&H in terms of the geometry and dimensions. The model consisted of a rectangular geometry with a total volume of 0.2 cm^3, whereas the gel was circular with a total volume of 1 cm^3. Despite such differences, some qualitative comparisons can be made to provide some assessment of the model's predictive capabilities.

First, S&H reported that the anisotropy in collagen fiber alignment that materialized between explants developed simultaneously (65). The models (for all cases) also predicted an increase in network anisotropy and alignment along the axis between explants, but anisotropy in the models did not develop simultaneously between explants. Instead, alignment increased first in the ECM networks adjacent to the explants and then spread outward until meeting at the midpoint between explants, provided the distance between explants was not too far (e.g., the two-explant model in Figure 2-2A). It is possible that the development of alignment between explants in the model proceeded gradually because the distance between explants in the model was greater than in the experiment. It is also possible that this discrepancy arose from some feature of the multi-scale model, such as the ECM network geometry used. Finally, it may be that the growth of fiber alignment outward from the explants did happen in the experiment, but that the changes in fiber alignment were too small to resolve with phase contrast microscopy and a 10x objective until a sufficient amount of reorganization had occurred, which would give the appearance of simultaneous fiber alignment.

Second, the strains developed during compaction for the three-explant model were highly dependent on the boundary conditions (Figure 2-3). For cases 1 and 2 where fixed boundaries were present, the maximum principal strains were directed parallel to the axis

23

between explants. In contrast, for case 3 (Figure 2-3C, F), where the surfaces were allowed to contract, the principal strains were generally directed perpendicular to the axis between explants. This strain pattern was consistent with the observations of S&H (65). They found that there was significant lateral but not axial movement of glass beads embedded in the gel between explants. The qualitatively similar strain pattern for case 3 indicates that free boundary conditions better reflected the experimental conditions of a gel spread out over a coverslip than the fixed boundary simulations did, and that a sufficient amount of translational freedom for the ECM network fibers was required to replicate the fiber restructuring of the experiment.

The model also predicted that a wide range of fibers strains developed in the ECM networks during uniaxial stretch. The inclusion of cell compaction changed the distribution of these strains, particularly in the regions around the cells where the highest strains were found, which could have important implications for predicting how macroscopic forces propagate down to the cellular level. In fact, the increasing use of mechanical stimulation to improve the mechanical properties of engineered tissues has necessitated the development of mechanical models that can predict the cellular mechanical environment as a function of the construct architecture, mechanical properties and macroscopic loading conditions. Like this model, these models have generally found that incorporating microscopic heterogeneity is important and that wide range of microscopic strains can develop when a given amount of macroscopic stretch is applied to a construct (16, 67, 68).

A number of simplifications that were made in this model must be acknowledged. First, the same constitutive relationship, microstructure, and material properties were

24

used for both the cellular and ECM networks as a matter of convenience, and because many of these parameters are not well defined experimentally, even though ECM proteins like collagen are formed and behave quite differently from intracellular cytoskeleton proteins like actin (69, 70). Other cellular details, including discrete cell attachments, cell proliferation, and cell migration, were omitted in this first-pass model. In addition, the method used here to simulate cell compaction was also chosen for its simplicity in implementation. It appears that uniform shrinking of fibers in the explants is sufficient for representing this aspect of the experimental system. It is far more probable, however, that cells pull on fibers until a homeostatic level of force is encountered, rather than until a set level of displacement is achieved (i.e. force limited versus displacement limited) (71). The next steps for developing this model involve modifying the details of the networks and the rules governing cell tractions so that they better reflect reality. For example, incorporating force-based rules for changing the fiber length based on target force should significantly change network restructuring and increase the development of anisotropy compared to the results presented here using uniform fiber shrinkage as a means to generate internal tension. To aid model development further, we are conducting new experiments (e.g. Figure 2-1A) so that we can better assess model predictions and the physics we are incorporating (including aspects of these simulations, such as the different explant geometries). In conclusion, the model predictions were consistent with experiments and demonstrate the model's potential for predicting fiber reorganization in response to cell traction forces.

25

CHAPTER 3

AN IMAGE-BASED MULTI-SCALE MODEL FOR A DIRECT COMPARISON WITH FIBRIN GELS EXPERIMENTS ON STUDYING THE ROLE OF CELL MATRIX INTERACTIONS IN WOUND HEALING

3.1 Introduction

Tissue growth, remodeling, and repair are complex processes that are regulated in part by multi-scale mechanical interactions. To better understand how these interactions contribute to the mechanobiology of the remodeling process in the context of wound healing and scar formation, we conducted *in vitro* experiments on fibroblast-matrix interactions in fibrin gels (as an approximation of the initially formed clot) subjected to either *Free* or *Fixed* in-plane mechanical constraints (8). Using averaged morphological measurements from the experiments, an idealized, image-based multi-scale model was used to simulate the experiment so that the ability of the model to capture the physics of short-term structural remodeling could be evaluated. Small, but significant, differences in short-term structural remodeling of fibrin gels by the fibroblasts in response to *Fixed* or *Free* gel boundaries were observed that could impact long-term remodeling. Image-based models of the experiments were able to qualitatively predict some features of the remodeling process. This combined system of experiments and image-based models represents a new model system for understanding the mechanobiology of scar formation and for devising and assessing new treatments to manage scar formation.

3.2 Methods

The focus of this chapter is to develop an image-based model of a series of *in vitro* experiments and compare the model's predictions to the experiment data. Details on the experimental portion of this work can be found in (8).

3.2.1 Multi-scale Model

Structural reorganization of the fibrin gel by the explants in the experiments was simulated with a multi-scale modeling technique that has been described in chapter 2. The expression for the macroscopic stress equilibrium is given as

$$\left\langle \sigma_{ij,i} \right\rangle + \sigma_{ij,i}{}^{nH} = \frac{1}{V} \oint_{\delta V} \left(\sigma_{ij} - \left\langle \sigma_{ij} \right\rangle \right) u_{k,i} n_k dA \tag{3.1}$$

where $\left\langle \sigma_{ij} \right\rangle$ is the macroscopic volume-averaged Cauchy stress of the fiber network, $\sigma_{ij}{}^{nH}$ is an additive neo-Hookean stress (defined below), σ_{ij} is the local microscopic stress, u is the displacement of the RVE boundary, and n is the unit normal vector to the boundary surface. The components of these stresses are related to the RVE volume, V, and the components of the position, x_i, and force, F_j, of the fiber nodes on the RVE boundary by equation (2.2). The force required to deform a fiber is calculated from a phenomenological constitutive equation (2.1) (72).

In order to limit the compressibility and distortion of the fibrin fiber networks, a continuum-level compressible neo-Hookean stress was added to the volume-averaged stress (c.f. (59)). This stress is given as

$$\sigma_{ij}^{nH} = \frac{G}{J} \left(B_{ij} - \delta_{ij} \right) + \frac{2G\nu}{J(1-2\nu)} \left(\ln(J) \right) \delta_{ij} \tag{3.2}$$

27

where G is the shear modulus, ν is Poisson's ratio, J is the determinant of the deformation tensor, and B is the left Cauchy-Green deformation tensor (73).

3.2.2 Model Formulation and Computational Details

In Chapter 2, we setup a multi-scale model of explant compaction of a collagen gel in which the FE domain was partitioned into cellular and extracellular matrix (ECM) domains (54). The effect of cell traction forces on the structural reorganization of the surrounding matrix was assessed by incrementally shortening the reference length of all the fibers in the cellular networks. The procedure generated tensile force in the cellular domain that induced substantial reorganization in the ECM networks in a manner dependent on the geometry of the problem. Here, image-based models were produced for direct comparison with the experiment as follows. First, a square FE mesh was created that matched the fibrin gel's dimensions of 8 mm x 8 mm x 0.8 mm (length, width, depth) and approximated the average geometric spacing and size of the triangular explants (Figure 3-1C, D). The mesh, which contained 46 elements along the length, 46 elements along the width, and four elements through the depth, consisted of 8,464 tri-linear hexahedral elements and 11,045 nodes (Figure 3-1). It was partitioned into a cellular domain consisting of three triangularly arranged squares, each consisting of 16 adjacent surface elements (i.e., one element through the depth), and a surrounding ECM domain. The model consisted of a collection of nearly isotropic 3D fiber networks that contained on average 337 ± 30 cross-linked fibers. Since experimental data about fiber realignment through the thickness was not available, network orientation and strength of alignment was quantified in a manner consistent with previous work using the 2D projections of the

28

3D microstructure as in equation (2.4), and the strength of alignment, α, is defined the same as in equation (2.5).
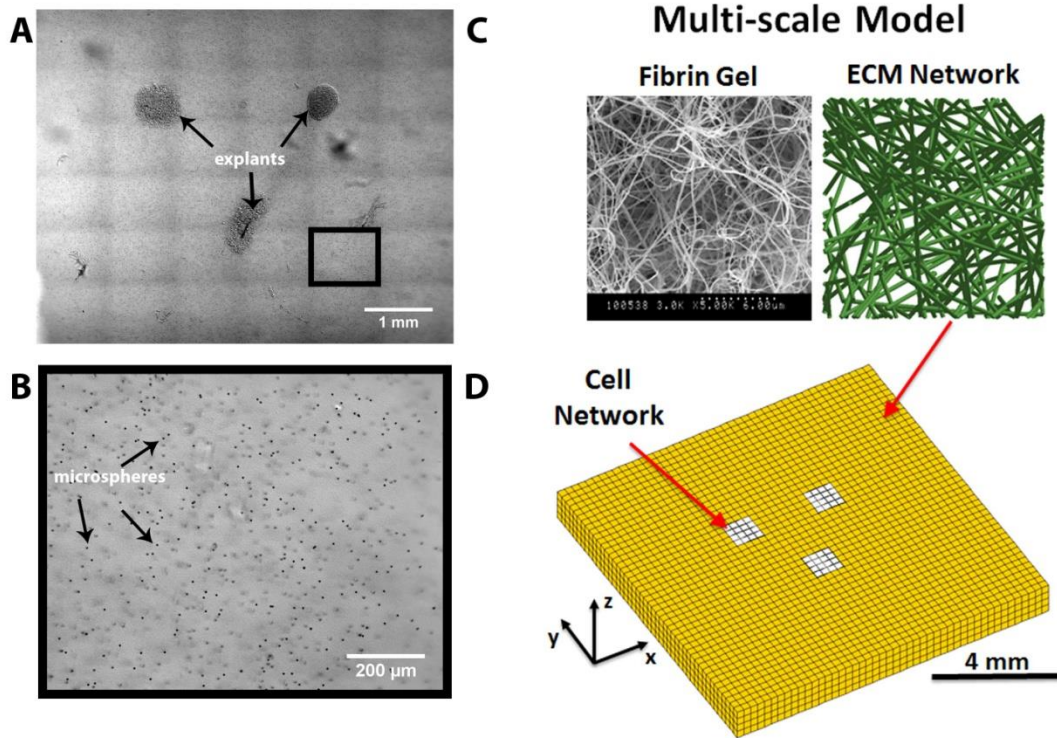
Figure 3-1: In vitro data collection and image-based computational model. (A) Three explants were placed at a distance of approximately 2 mm from each other to form the vertices of a triangle. A tiled image consisting of 36 individual 10x DIC images was acquired every 15 minutes in order to observe and quantify structural and morphological changes in the fibrin gel. (B) Over the course of the experiment the instantaneous and cumulative displacements of a subset of embedded microspheres was analyzed at each location (the depicted image corresponds to the black box in (A)). (C) The image-based computational model consists of finite elements containing fiber networks that are representative of the fibrin fibers in the gel. (D) The model is partitioned into cellular networks (white elements) and surrounding fibrin networks (yellow elements) that are configured to approximate the geometric configuration of the explants and gel in the experiments.

Image-based models of the experiment were constructed by using the average explant area and the centroid-to-centroid distances (*Free* and *Fixed* gels combined) at the start of the experiment as target values for the model. These values were not matched exactly due to the discrete nature of the elements and computational constraints on

29

increasing the number of elements. As a result, the simulated explant area was given a value of 0.484 mm^2 compared to an average initial explant area in the experiments of 0.463 ± 0.089 mm^2 (average of both *Free* and *Fixed* cases). Similarly, the horizontal centroid-to-centroid distance, which was larger between the top two explants, was set at 2.09 mm compared to 2.2 ± 0.15 mm in the experiment. The centroid-to-centroid spacing of the other two axes were set to 2.03 mm in the model compared to a spacing of 2.03 ± 0.12 mm and 1.93 ± 0.21 mm in the experiment.

To simulate the *Fixed* experiment, all FE mesh surfaces except the top surface, which remained free, were fixed. To simulate the *Free* experiment, the only constraint on the FE mesh was on the bottom surface, where the nodes contained in an area at the center measuring 1.74 mm x 1.74 mm were fixed. The surrounding elements were allowed to translate inward in a manner consistent with the small reduction (< 2%) in gel area observed experimentally, where the gel became partially detached from the substrate around the periphery. Structural remodeling due to explant traction forces was simulated by incrementally reducing the reference lengths of all of the fibers in the cellular networks uniformly by 24%. This value was selected so that the simulated final average area of an explant matched the average measured area of the explants for the *Free* boundary condition after 24 hours in the experiments. The *Free* condition was selected because the decrease in explant area was slightly greater in the *Free* boundary case than in the *Fixed* boundary case. Both cell and gel networks were assigned values of $E_f A_f = 3 \times 10^{-10} N$ and $B = 4$, and $G = 1$ Pa and $\nu = 0.3$ for the neo-Hookean component. These values were obtained by fitting a model to the stress-strain curve generated from a uniaxial mechanical test of a rectangular 6.8 mg/ml fibrin gel.

30

The computational costs associated with the simulations were very large. There were roughly 1,000 degrees of freedom per fiber network and 67,712 networks in each mesh. As a result, simulations were run using a custom parallelized C code with message passing interface (MPI) on high performance computing resources (ITS Helium Cluster, University of Iowa). Simulations were executed on a single 12-core node (Intel Xenon processor with 144 GB of memory and Infiniband connectivity). The fixed boundary condition simulation required a CPU time and wall time of 282 hours and 58 hours, respectively. The CPU time and wall time for the free boundary condition simulation were 348 hours and 74 hours, respectively.

3.3 Results

Model predictions for both *Fixed* and *Free* boundary conditions resulted in qualitatively similar morphological changes as in the experiment (Figure 3-2). For the *Free* condition, the simulation was terminated when the final explant area shrank to 66% of its initial area to 0.319 ± 0.001 mm^2, in close agreement with the experiment ($66.6\% \pm 17.9\%$ and 0.31 mm$^2 \pm 0.07$ mm^2, respectively). For the same amount of simulated compaction, the explant area in the *Fixed* condition reduced to 69% of the initial area to 0.332 ± 0.002 mm^2, also in close agreement with the experiment ($70.9\% \pm 19.9\%$ and 0.33 mm$^2 \pm 0.12$ mm^2, respectively). The centroid-to-centroid distances shortened to $97.1\% \pm 0.2\%$ and $99.2\% \pm 0.0\%$ the initial distances in the *Free* and *Fixed* simulations, respectively, but these changes in distance were not as much as in the experiment. In the experiments, the explants also moved closer to each other in a manner dependent on the boundary conditions. The average centroid-to-centroid distance between explants after 24

31

hours, normalized with the corresponding distance between explants at $t = 0$ hours, was lower in *Free* gels (0.95 ± 0.02) compared to *Fixed* gels (0.98 ± 0.02).

Model predictions of displacements in the gel were also qualitatively similar to the experiments in several ways (Figure 3-2). First, the overall patterns of the displacement fields were similar, with the largest displacements occurring in regions closest to the explants. In addition, much larger displacements were predicted in the *Free* condition compared to the *Fixed* condition.
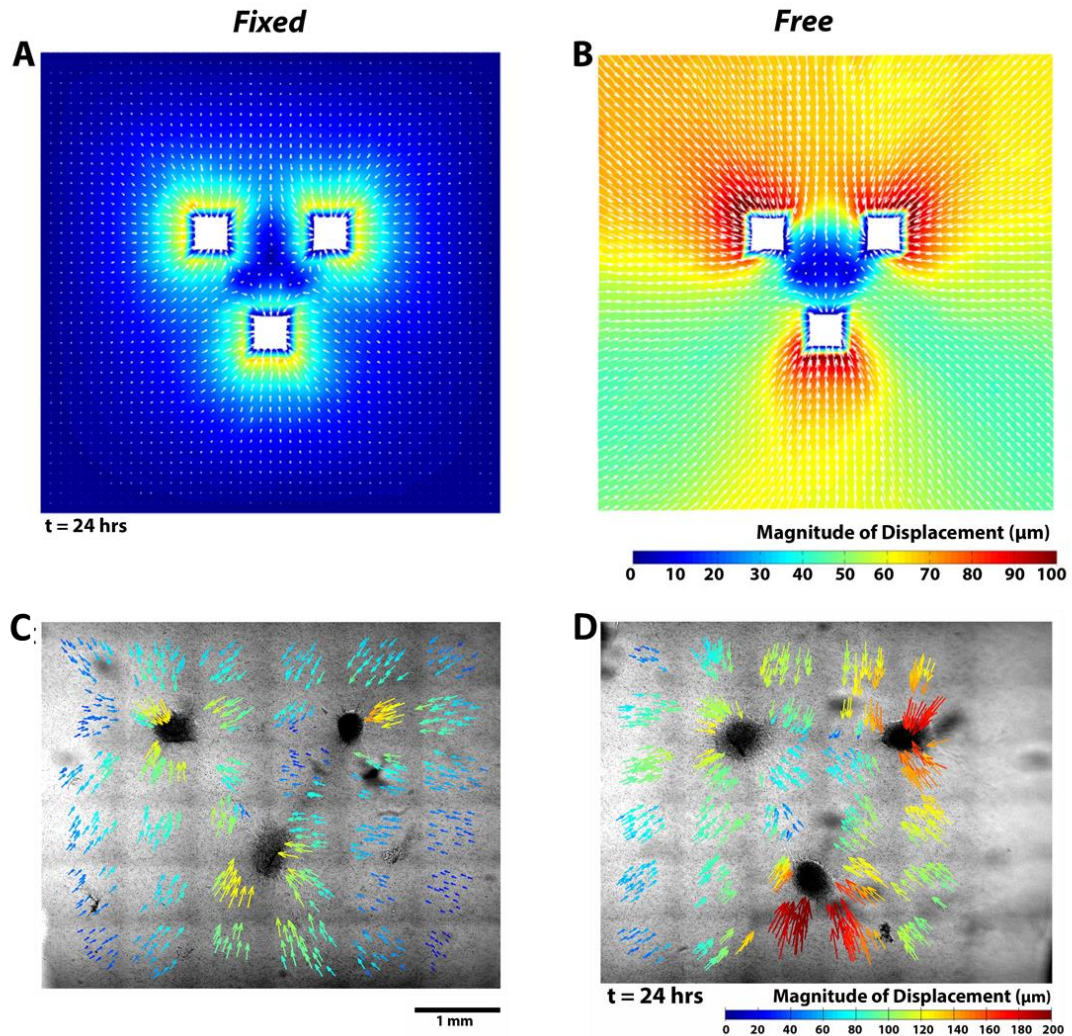
Figure 3-2: Model predictions (A, C) and experimental data (B, D) of displacement. Displacement fields for (A, C) the Fixed and (B, D) Free conditions at 24 hours. Arrows indicate the direction of ECM displacement towards the compacting explants.

32

Model predictions of fiber network reorganization were also similar to those observed experimentally (Figure 3-3). For both *Fixed* and *Free* gels, changes in the strength of fiber alignment ($\Delta\alpha$) were greatest around the explants and in the axial regions between explants (Figure 3-3 C, D). Fiber networks located away from the explants were mostly unaffected and remained close to isotropic in both conditions (Figure 3-3 E, F). Although the fiber alignment patterns between the two simulations were similar, small differences were predicted. In the *Free* gel, more surface ECM elements had a change in the initial strength of fiber alignment $\Delta\alpha > 0.05$ than in the *Fixed* gel (281 versus 234, respectively). In addition, the overall average $\Delta\alpha$ was slightly higher in the *Free* gel (0.0278 ± 0.0353) than in the *Fixed* gel (0.0216 ± 0.0357), but the overall α was the same at 0.1506 ± 0.0738 and 0.1505 ± 0.0736 in the *Free* and *Fixed* gel, respectively. In contrast, network fiber forces were higher in the *Fixed* gel (1.3 ± 8.6 pN) than in the *Free* gel (0.5 ± 6.3 pN). Also, even though the symmetry of the model resulted in strong axial alignment between all three explants, greater spacing between the top two explants than with the bottom explant resulted in significantly lower average fiber alignment strength ($\alpha = 0.134 \pm 0.061$ and $\alpha = 0.133 \pm 0.063$ in the *Fixed* and *Free* gels, respectively) than in the other axial regions ($\alpha = 0.279 \pm 0.080$ and $\alpha = 0.268 \pm 0.055$ in the *Fixed* gel, and $\alpha = 0.276 \pm 0.077$ and $\alpha = 0.266 \pm 0.054$ in the *Free* gel).
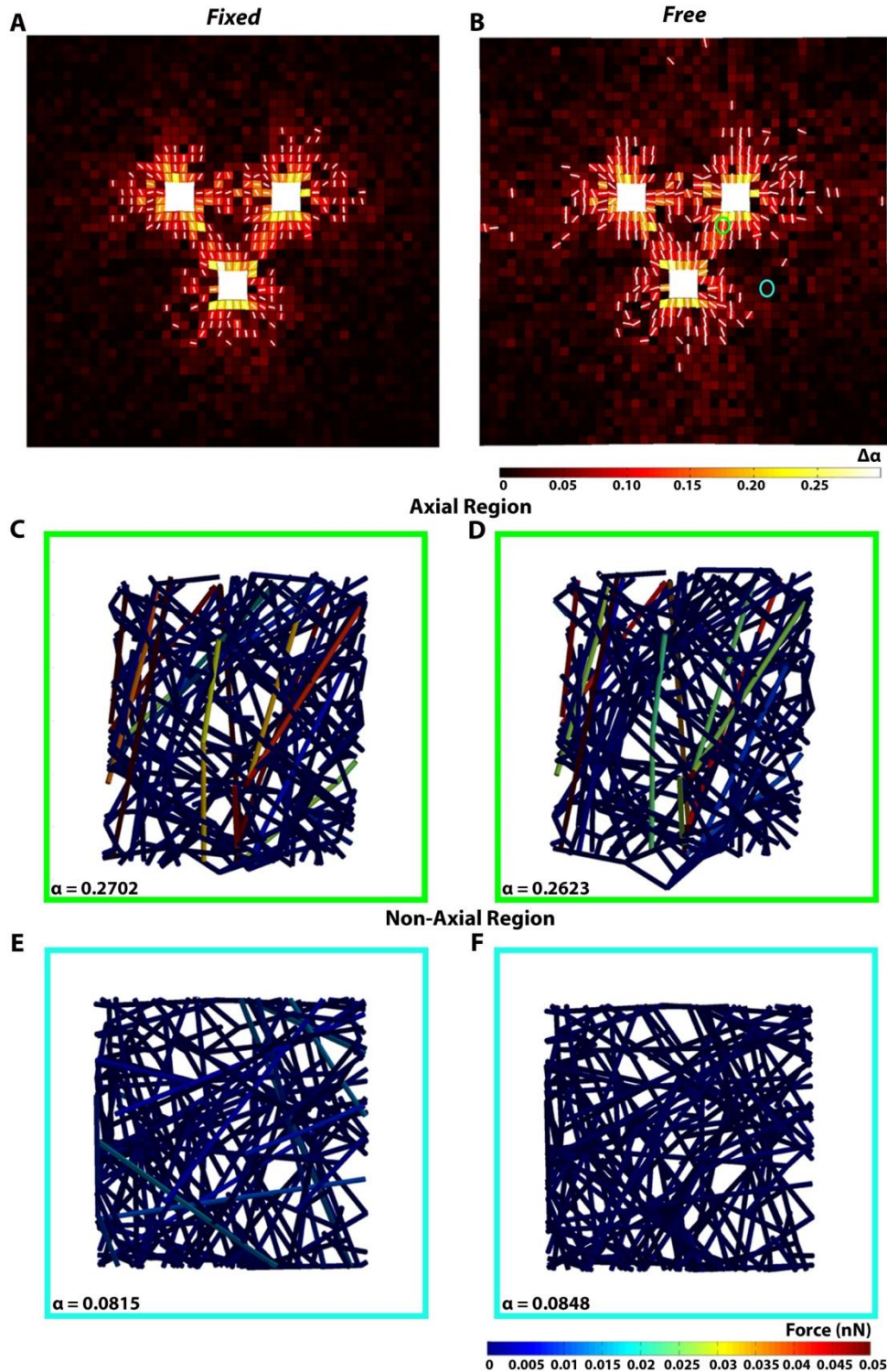
Figure 3-3: Model prediction of fiber realignment. Fiber network realignment at t = 24 hours for a (A) Fixed and (B) Free gel. The color map indicates the change in the strength of fiber alignment ($\Delta\alpha$) from the initial network configuration. Also shown as white arrows are the principal directions of fiber alignment for those elements where $\Delta\alpha > 0.05$. Network reorganization and fiber forces for a representative network in an axial (C,D) and non-axial region (E,F).

3.4 Discussion

The image-based computational models were able to predict boundary condition dependent relative changes in explant morphology and spacing, regional differences in microsphere displacements, and fiber alignment patterns that qualitatively matched what was observed experimentally. However, the model predicted much lower displacement magnitudes and an increase in the period average rates of displacement over time instead of a decrease. Small differences in fiber alignment between the *Free* and *Fixed* gels were also predicted, but the imaging method used did not clearly show whether such differences in alignment between gels existed or not. Instead, these images showed stronger alignment in axial regions between explants than in non-axial regions, and that one or two dominant axes of fiber alignment formed instead of three, regardless of the boundary conditions. As stated earlier, formation of a dominant axis of alignment in the experiments could be a result of asymmetries in the experiment, such as the centroid-to-centroid distance or the size/number of cells, and thus the total force associated with each explant. The model did predict less alignment in the matrix between the top two explants, which were farther apart from each other than with the bottom explant, than between each of the top explants and the bottom one, which is consistent with our experimental observations that dominant axes form between explants that are closer together.

Several model refinements could potentially improve model predictions. For one, the description of the microstructure could be improved to better reflect the micromechanics of fibrin fibers in the gel. Currently, network fibers are represented as single segments that are cross-linked to other fibers via ball joints that cannot resist

35

moments. Others have represented network fibers as a series of connected segments with torsion springs at the joints that resist rotation (23, 74, 75). This representation allows for curved fibers that can collapse locally yet still transmit tension as they are gathered into a pericellularly dense region around the explants. Some of these models have reproduced this densification and the development of alignment between pairs of cells (23, 75). Incorporating such behavior into our model should increase the predicted cumulative displacements and also help match the fibrin densification observed experimentally.

Another area requiring improvement is in modeling the manner in which cells generate and respond to forces. In the model, cell traction forces are generated by incrementally shortening the reference length of cellular network fibers the same amount at each step. This approach does capture the alignment produced and relative differences in cumulative displacements, but predicted rates of displacement continued to increase over time, which is in opposition to the experimentally observed decrease with time. This behavior suggests that the cells are modulating how much they deform the surrounding matrix based on either a feedback-controlled, force-sensing mechanism, or possibly by saturation of the number of cell-ECM binding sites (76). Others have modeled the development of traction forces with the former mechanism in mind (77, 78). For example, Wang et al. incorporated the well-known Hill-relation used to describe muscle contraction (79). We anticipate that incorporating similar changes into the model will result in a decrease in the rate of displacement with time and better predict the short-term remodeling observed experimentally. Finally, although it was beyond the scope of this work, a mechanism for degrading the fibrin fibers and replacing it with collagen fibers

36

will also be necessary in order to predict long–term remodeling and propensity for scarring.

3.5 Conclusion

Multi-scale mechanical interactions in wound healing are poorly understood. They are particularly important to characterize because they control both the manner in which mechanical signals are propagated to the cellular level to direct cell activity and the ultimate mechanical behavior and function of the healed tissue. Due to the complexity of these processes, it is necessary to develop computational models that serve as a theoretical basis for predicting how ECM remodeling proceeds. In this study, we began the development of this kind of modeling system by quantitatively characterizing small but significant differences in an *in vitro* explant-fibrin gel system with *Fixed* and *Free* in-plane mechanical constraints. We also performed a rigorous comparison with an image-based multi-scale mechanical model and found qualitative agreement with the experiments in some areas. Discrepancies between model and experiment provide fertile ground for challenging model assumptions and devising new experiments to enhance our understanding of how this multi-scale system functions. These efforts will ultimately improve the predictions of the remodeling process, particularly as it relates to dermal wound healing and the reduction of patient scarring. Such models could then be used to recommend patient-specific mechanical-based treatment dependent on parameters such as wound geometry and location and patient age and health.

CHAPTER 4

FIBER NETWORK MODELS PREDICT ENHANCED CELL

MECHANOSENSING ON FIBROUS GELS

4.1 Introduction

The propagation of mechanical signals through non-linear fibrous tissues is much more extensive than through continuous synthetic hydrogels. Results from recent studies indicate that increased mechanical propagation arises from the fibrous nature of the material rather than the strain-stiffening property (12, 14, 15). The relative importance of different parameters of the fibrous network structure to this propagation, however, remain unclear. In this chapter, we directly compared the mechanical response of substrates of varying thickness subjected to a constant cell traction force using either a non-fibrous strain-stiffening continuum-based model or a volume-averaged fiber network model consisting of two different types of fiber network structures: one with low fiber connectivity (*Growth Networks*) and one with high fiber connectivity (*Delaunay Networks*). The *Growth Network* fiber models predicted a greater propagation of substrate displacements through the model and a greater sensitivity to gel thickness compared to the more connected *Delaunay Networks* and the nonlinear continuum model. Detailed analysis of the results indicates that rotational freedom of the fibers in a network with low fiber connectivity is critically important for enhanced, long-range mechanosensing. Our findings demonstrate the utility of multi-scale models in predicting cells mechanosensing on fibrous gels, and they provide a more complete understanding of how cell traction

38

forces propagate through fibrous tissues, which has implications for the design of engineered tissues and the stem cell niche.

4.2 Methods

In this chapter, we comprehensively compare a continuum-based finite element (FE) model (*Continuum* model) that uses a third-order strain energy density function to describe material nonlinear strain stiffening behavior with a multi-scale fiber network FE model (*Fiber* model) that consists of a set of fiber networks that are either characterized as *Growth Networks* or *Delaunay Networks* (c.f., "*Continuum Model*" & "*Fiber Model*" sections, respectively). The nonlinear response of the Fiber model primarily derives from non-affine rotations and stretch of the individual cross-linked fibers of the network. To facilitate direct comparisons between the different types of models formulated to describe different physical attributes of the system, the parameters governing each model were selected so that the shear stress-strain response of each model matched the macroscopic mechanical behavior of a 2mg/mL acellular fibrin gel (data obtained from Wen *et al.* (80)) representative of those used as substrates for the study of cell mechanosensing.

4.2.1 Models and Boundary Conditions

The propagation of cell traction forces through deformable substrates of increasing thickness was assessed by considering one-element wide, rectangular FE meshes representing a spatial scale of 75 µm x 4 µm x (10 – 200) µm (length, width, thickness). Three FE meshes consisting of tri-linear hexahedral elements were created in

39

ABAQUS CAE (v. 6.12-1; ABAQUS, Providence, RI). These meshes had thicknesses of 10 µm, 30 µm, 50 µm, and 200 µm respectively.

A schematic of the model is shown in Figure 4-1. It depicts a single cell applying a constant inward traction force on the surface of a finite thickness gel. The model possesses axes of symmetry on the left surface and the front and back surfaces. For the left surface, the nodes were fixed in x and z and free in y (i.e., nodes were free to move up and down through the thickness). For the front and back surfaces, the nodes were fixed in z and free in x and y (i.e., nodes were free to move along the length and thickness). For the bottom and right surfaces, the nodes were fixed in x, y, and z, and for the top surface nodes were free in x, y, and z. A small subset of 22 nodes on the top surface was designated as focal adhesion nodes contained with the focal adhesion area at the front of the cell. A total cell traction force of 6 nN, which is equivalent to a cell traction stress of about 250 Pa (within the range of those reported from traction force microscopy studies (81, 82)), was applied to these nodes by equally dividing this total force amongst the nodes and over 55 equally spaced steps. A region on the top surface starting 9 µm from the left surface and extending an additional 6 µm in length was designated as the focal adhesion area for comparison with our previous work (12). Since large stress gradients develop in this region, the mesh in this area (a region measuring 24 µm x 5 µm (length, thickness)) was locally refined until there was less than a one percent change in the total nodal displacement at the end of the simulation with further mesh refinement.
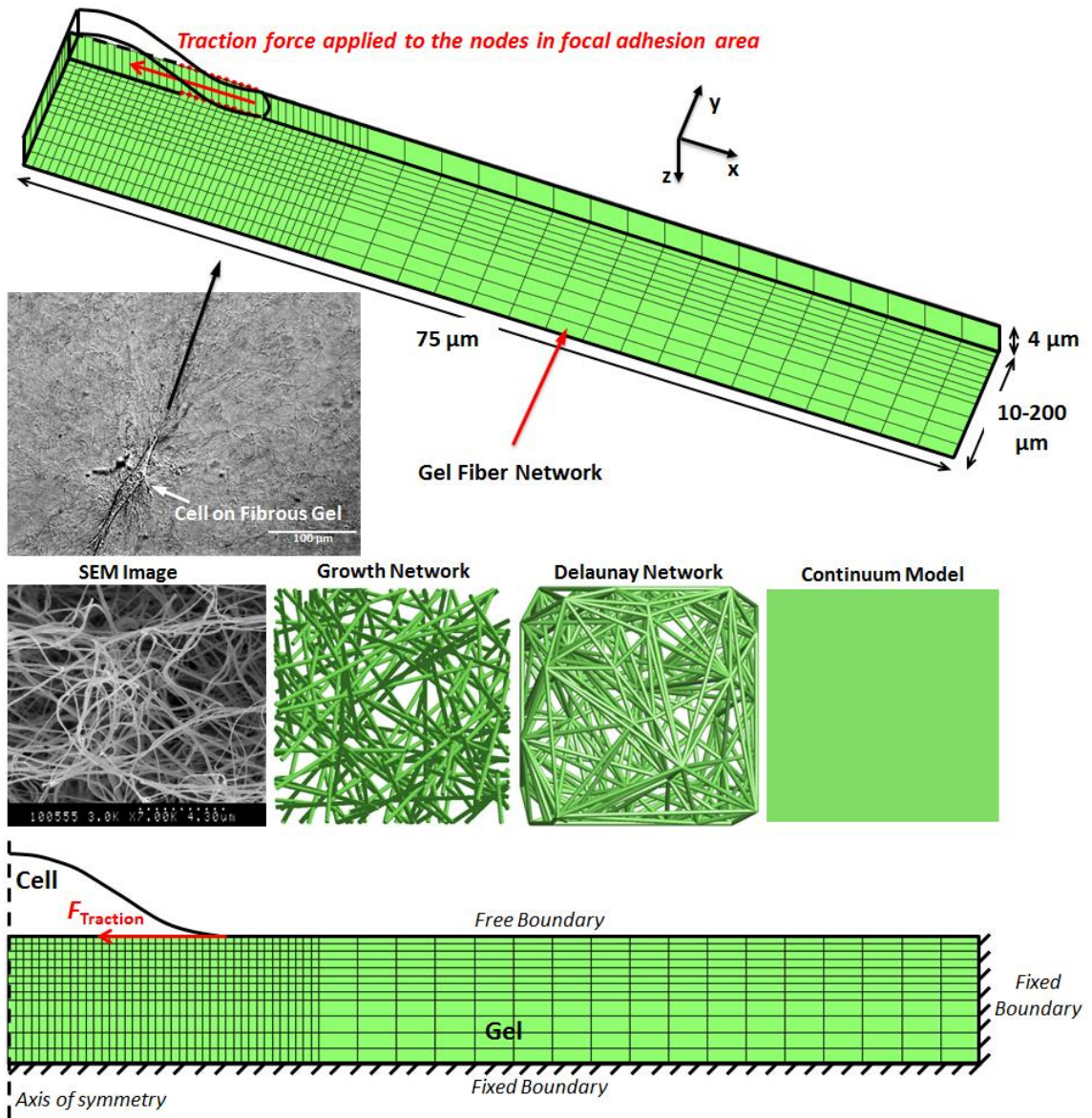
Figure 4-1: Schematic of the FE model. Cell traction forces are applied to the FE nodes (red) associated with the focal adhesion area on the FE top surface. For the fiber model, 3D *Growth* or *Delaunay* fiber networks similar to the microstructures found in fibrous gels were used instead and compared to the nonlinear *Continuum* model.

4.2.2 Continuum Model

The effects of material nonlinearity (strain stiffening) were investigated using FE models constructed in ABAQUS (v. 6.12-1; ABAQUS, Providence, RI) with C3D8 (tri-

linear hexahedral) elements. We selected a third-order (cubic) reduced polynomial strain energy function given by

$$W = C_{10}(I_1 - 3) + C_{20}(I_1 - 3)^2 + C_{30}(I_1 - 3)^3 + \frac{1}{D_1}(J^{el} - 1)^2 + \frac{1}{D_2}(J^{el} - 1)^4 +$$

$$\frac{1}{D_3}(J^{el} - 1)^6 \tag{4.1}$$

where W is the strain energy density, I_I is the first strain invariant, C_{10}, C_{20} and C_{30} are material constants, D_1, D_2 and D_3 are compressibility terms, and J^{el} is the elastic volume strain (83). We selected this strain energy function because it is of the same form as the third order reduced polynomial used in our earlier preliminary investigation, and it is able to match the nonlinear stiffening behavior of fibrous gels (12). We refer to this model throughout the manuscript as the Continuum model.

4.2.3 Fiber Model

The Fiber model employed herein uses a multi-scale modeling framework that has been described in chapters 2 and 3.

Fiber Networks

The microscale is represented by a set of cross-linked fiber networks that are centered at the integration points of the FE elements. Two microstructurally distinct types of networks were investigated in this study. The first type of network is referred to as a *Growth Network* because the algorithm used to produce the network follows rules that are based on a process by which monomeric biomolecules may stochastically self-assemble into fibers (c.f. (57)). The second type of network we investigated is referred to as a *Delaunay Network* because the networks are generated from Delaunay triangulation (84).

42

Both types of networks were constructed in MATLAB, and a collection of distinct networks with the following properties were obtained:

Growth Network Model: Networks containing 338 ± 30 cross-linked fibers, with non-dimensional individual fiber lengths of 0.28 ± 0.23, a total non-dimensional fiber length of 94.79 ± 7.21, a fiber connectivity of 3 (i.e., the number of fibers connecting at a crosslink), and 3D orientation tensor (defined below) eigenvalues of 0.29 ± 0.02, 0.33 ± 0.01, and 0.38 ± 0.02.

Delaunay Network Model: Networks containing 470 ± 9 cross-linked fibers, with non-dimensional individual fiber lengths of 0.38 ± 0.16, a total non-dimensional fiber length of 178.35 ± 6.49, a fiber connectivity of 13.26 ± 3.75, and 3D orientation tensor eigenvalues of 0.31 ± 0.01, 0.33 ± 0.01, and 0.36 ± 0.01.

Three-dimensional fiber network orientation and strength of alignment can be quantified with the length-weighted orientation tensor, Ω_3, defined as

$$\Omega_3 = \frac{\sum_{i=1}^{NF} l_i \begin{bmatrix} \cos^2\theta_i \sin^2\varphi_i & \cos\theta_i \sin\theta_i \sin^2\varphi_i & \cos\theta_i \sin\varphi_i \cos\varphi_i \\ \cos\theta_i \sin\theta \sin^2\varphi_i & \sin^2\theta_i \sin^2\varphi_i & \sin\theta_i \sin\varphi_i \cos\varphi_i \\ \cos\theta_i \sin\varphi_i \cos\varphi_i & \sin\theta_i \sin\varphi_i \cos\varphi_i & \cos^2\varphi_i \end{bmatrix}}{\sum_{i=1}^{NF} l_i}$$

(4.2)

where l_i is the length of fiber i, θ_i is the angle fiber i makes with the horizontal axis in the *x-y* plane, φ_i is the angle the fiber i makes with the *z*-axis, and the sum is over all of the fibers, *NF*, in the network. The eigenvalues and eigenvectors of Ω then correspond to the magnitudes and principal direction of network fiber alignment, respectively, with an isotropic network possessing eigenvalues of [0.33 0.33 0.33] and a completely aligned network possessing eigenvalues of [0 0 1]. Networks in this study were produced so that they were nominally isotropic in all three dimensions. To facilitate visualization, changes

43

in fiber organization and alignment in response to cell traction were quantified using the two-dimensional orientation tensor, Ω_2, which is given as:

$$\Omega_2 = \frac{\sum_{i=1}^{NF} l_i \begin{bmatrix} \cos^2 \theta_i & \cos \theta_i \sin \theta_i \\ \cos \theta_i \sin \theta_i & \sin^2 \theta_i \end{bmatrix}}{\sum_{i=1}^{NF} l_i} \tag{4.3}$$

The three-dimensional tensor reduces to the two-dimensional tensor when $\varphi = 90°$. The degree of anisotropy, α, a metric of strength of network fiber alignment, can be defined as $\alpha = 1 - \omega_1/\omega_2$, where ω_1 and ω_2 are the minor and major eigenvalues of Ω, respectively. Here, the eigenvalues for an isotropic network corresponds to [0.5 0.5] and $\alpha = 0$, and for a completely aligned network these values correspond to [0 1] and $\alpha = 1$ (85). The change in fiber alignment with respect to the initial network configuration can also be defined as $\Delta\alpha = \alpha - \alpha_{initial}$, where $\alpha_{initial}$ is the initial strength of network fiber alignment.

Model Parameters

Model parameters were selected in order to match the mechanical behavior of a 2 mg/mL acellular fibrin gel in simple shear (12, 13). *Continuum* and *Fiber* models (described below) were subjected to equivalent boundary conditions and deformations as described in the experiment. Model parameters were selected until the mechanical response fit the experimental data of the test (Figure 4-2).

44
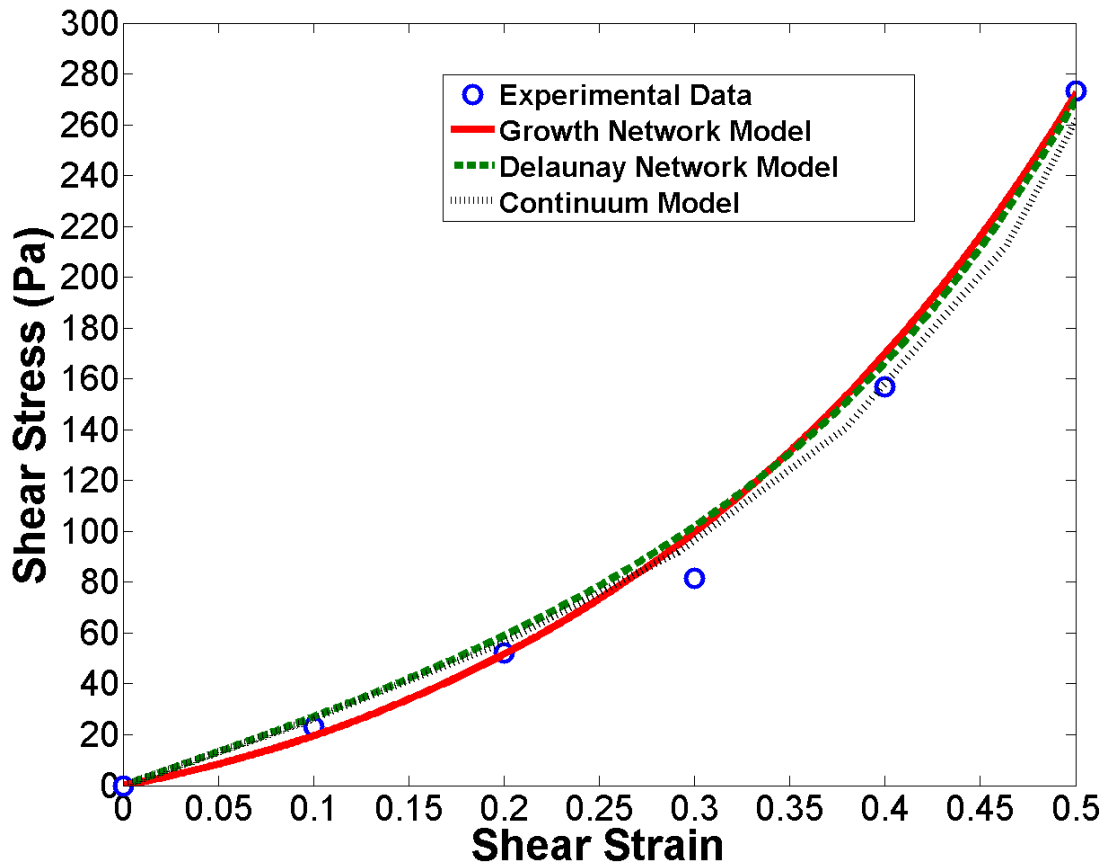
Figure 4-2: Shear simulation results fitted to experimental data for a 2 mg/mL acellular fibrin gel from Wen *et al*. (80). Model parameters were selected to match the nonlinear increase in stress with strain.

Effective Stiffness

The stiffness the cell "senses" as a function of the substrate mechanical properties and thicknesses was assessed by calculating the effective stiffness of the system, k_{eff}. Effective stiffness describes a substrate's resistance to deformation upon application of a shear force on the surface of the substrate; this stiffness can differ from the bulk modulus of the substrate due to material nonlinearity and/or fiber interactions. Here effective stiffness was calculated in a manner analogous to that of Mehrotra *et al*. (86) as:

45

$$k_{eff} = \frac{F/A}{\bar{u}/\bar{R}} \propto \frac{1}{\bar{u}} \tag{4.4}$$

where F is the total traction force exerted by the cell on the substrate, A is the undeformed focal adhesion area, $\bar{u}$ is the mean displacement of the nodes, and $\bar{R}$ is the mean radius of the focal adhesion area. Note that in all models the force boundary conditions were constant and the only variable that changed was $\bar{u}$. Thus, for the given traction force applied, a lower displacement at the "focal adhesions" resulted in a higher effective stiffness.

Computational Resources

Due to the substantial computational costs associated with the large number of degrees of freedom in the *Fiber Network* models (i.e., eight fiber networks in each element with more than 1000 degrees of freedom per network) simulations were run using a custom parallelized C code with message passing interface (MPI) on high performance computing resources (ITS Helium Cluster, University of Iowa) utilizing a single 12-core node (Intel Xenon processor with either 24 GB or 144 GB of memory and Infiniband connectivity). The CPU time and wall time for these simulations ranged from approximately 18 hours to 1128 hours and from 4 hours to 227 hours, respectively, depending on the job size. All *Continuum* models were run in ABAQUS and all post processing was done using MATLAB on a local coreTM i7-2600 HP desktop computer.

4.3 Results

The simulation cases considered in this study were designed to ask the following questions: (1) does the experimentally observed long-distance sensing of cells on fibrous

46

gels originate from nonlinearity in the bulk material properties or from some aspect of the fiber structure, and (2) if it is the fiber structure how do differences in idealization of the microstructure affect model predictions. To answer the first question we compared the *Continuum* model to a *Growth Network Fiber* model, and to answer the second question we compared a *Growth Network Fiber* model to a *Delaunay Network Fiber* model.

Comparison between Continuum Model and Growth Network Fiber Model

Material parameters were selected for each model (Table 4-1) so that the simulated shear stress-strain curves approximated an experimentally generated fibrin gel shear stress-strain curve up to a shear strain of 50% (Figure 4-2). The material properties were chosen for each model to match the fibrin gel's nonlinear response at low to mid-level strains because the shear strains developed in the simulations for the applied cell traction force were less than 40%.

Table 4-1: Material parameters values used for each model.

Continuum Model:	C_{10} = 130 Pa; C_{20} = 120 Pa; C_{30} = 125 Pa; v = 0.49
Growth Network Model:	$E_f A_f$ = 45 nN; B = 0.2; G = 10 Pa; v = 0.49
Delaunay Network Model:	$E_f A_f$ = 1.5 nN; B = 3; G = 10 Pa; v = 0.49

Application of a constant horizontal cell traction force on the gel surface produced comparable magnitudes and patterns in the stress (Figure 4-3) and displacement fields (Figure 4-4) between the *Continuum* and *Growth Network* models for all thicknesses. The largest maximum principal stresses were found in the focal adhesion (FA) area in all models. The average principal stresses in this region were lower in the *Continuum* model were approximately 30% to 40% lower than in the *Growth Network* model for all thicknesses (Table 4-2). The largest displacements in the models were also found in the

47

FA area. These displacements were between 1.7 and 2.1 times lower in the *Continuum* model than in the *Growth* model and increased with increasing gel thickness.
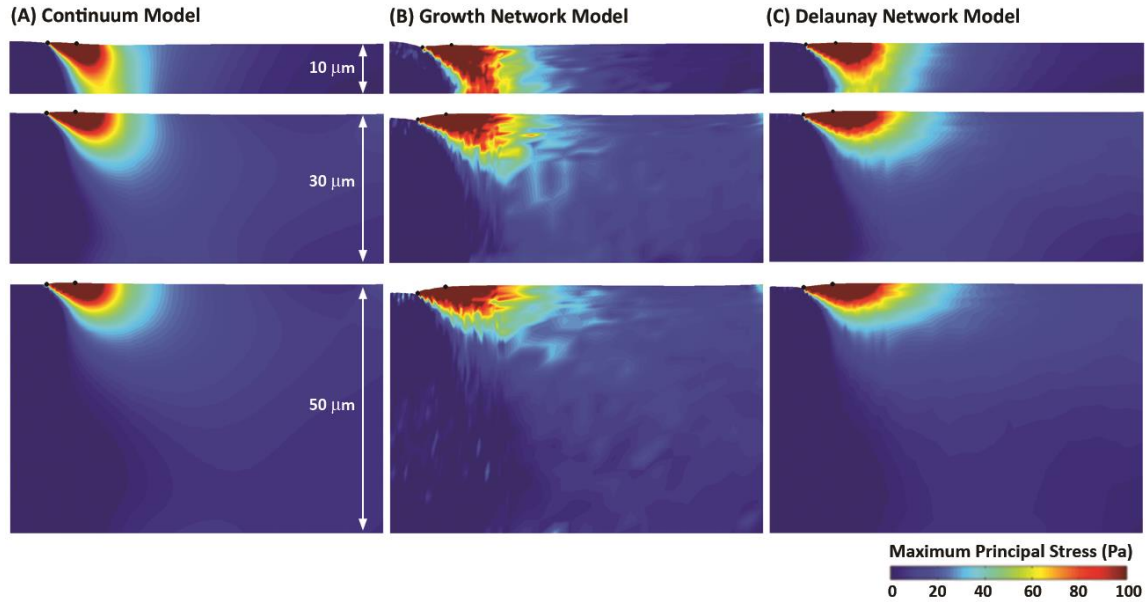
Figure 4-3: Maximum principal stress for 10 µm, 30 µm, and 50 µm thick gels in response to 6 nN of traction force. Stress contours for the (A) *Continuum* model, the (B) *Growth Network* model, and the (C) *Delaunay Network* model. Black nodes correspond to the inner and outer nodes of the focal adhesion area where the traction forces were applied.

Table 4-2: Average principal stress and displacements in focal adhesion (FA) regions.

	Thickness [µm]	Continuum	Growth	Delaunay
Principal Stress [Pa]	10	266 ± 119	366 ± 204	368 ± 199
	30	278 ± 124	420 ± 206	385 ± 190
	50	277 ± 122	444 ± 191	387 ± 192
	200	275 ± 121	445 ± 175	391 ± 183
FA Displacement [µm]	10	1.7 ± 0.1	2.9 ± 0.2	2.1 ± 0.1
	30	2.0 ± 0.2	3.9 ± 0.2	2.5 ± 0.1
	50	2.1 ± 0.2	4.2 ± 0.2	2.6 ± 0.1
	200	2.1 ± 0.2	4.5 ± 0.2	2.7 ± 0.1
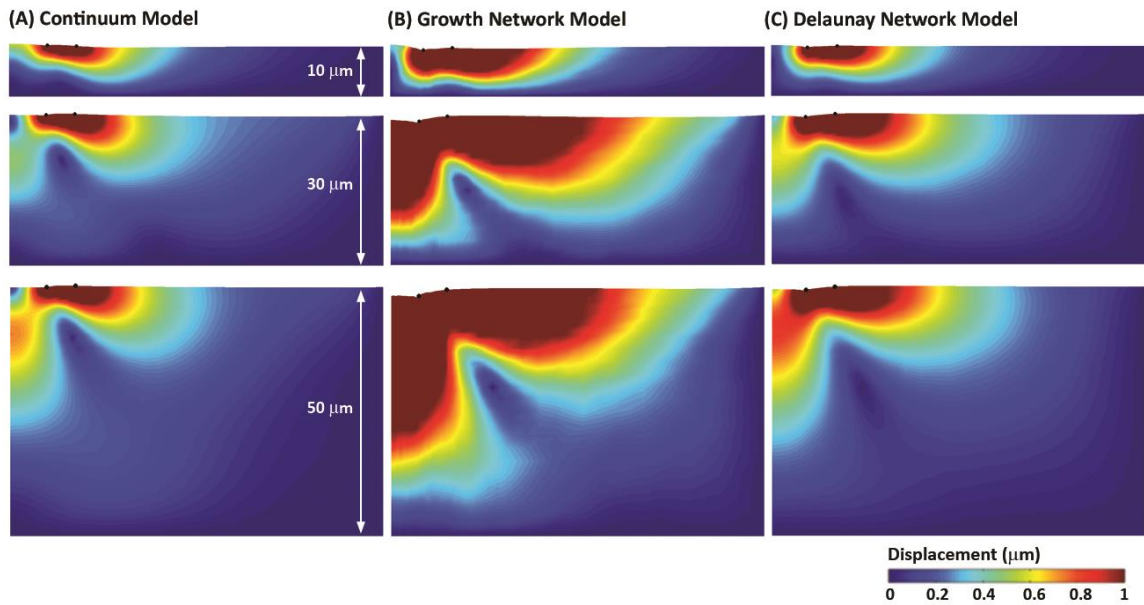
Figure 4-4: Displacement fields for 10 µm, 30 µm, and 50 µm thick gels in response to 6 nN of traction force for the (A) *Continuum* model, the (B) *Growth Network* model, and the (C) *Delaunay Network* model. Black nodes correspond to the inner and outer nodes of the focal adhesion area where the traction forces were applied.

A closer look at the nodal displacements along the length of the top surface of 10 µm, 30 µm and 50 µm thick gels can be found in Figure 4-5. Here, it can be seen that the nodal displacement magnitudes for the models were highest in the FA area (indicated by the gray band), and were substantially larger and extended laterally much farther for the *Growth Network* model. Peak nodal displacement magnitudes increased with gel thickness for all models, with the most pronounced increases occurring for the *Growth Network* model. As a result, the effective stiffness was much lower for the *Growth* model compared the *Continuum* model (Figure 4-6A). The sensitivity of effective stiffness to substrate thickness was further assessed by normalizing effective stiffness by the asymptoting values obtained at 200 µm (Figure 4-6B). Although effective stiffness in both models decreased with increasing substrate thickness, the *Growth Network* model

49

was much more sensitive to changes in the gel thickness than the *Continuum* model. Effective stiffness in the *Growth Network* model decreased 26% from 10 µm to 30 µm compared to a 15% decrease over the same range for the *Continuum* model, 7% compared to 5% from 30 µm to 50 µm, and 7% compared to 0% from 50 µm to 200 µm, respectively.
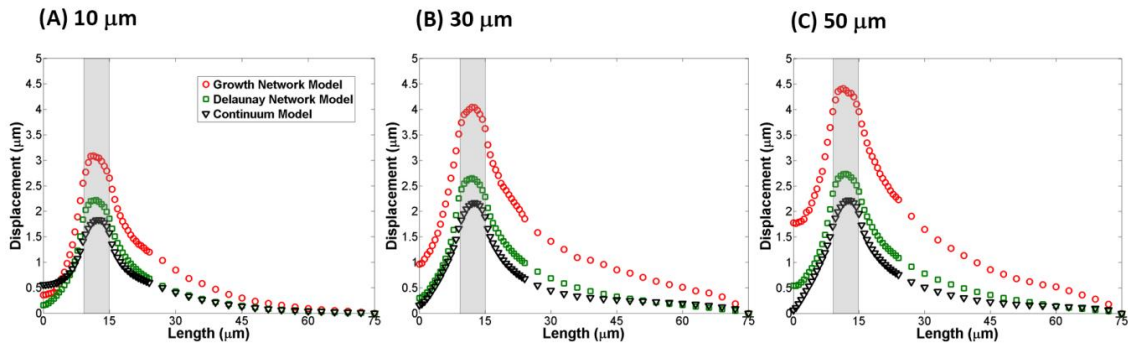
Figure 4-5: Magnitude of displacement along the length of the FE domain for nodes at the top surface of (A) 10 µm, (B) 30 µm, and (C) 50 µm thick gels for the *Growth Network*, *Delaunay Network* and *Continuum* models. Shaded regions indicate which FE nodes were associated with the focal adhesion area.
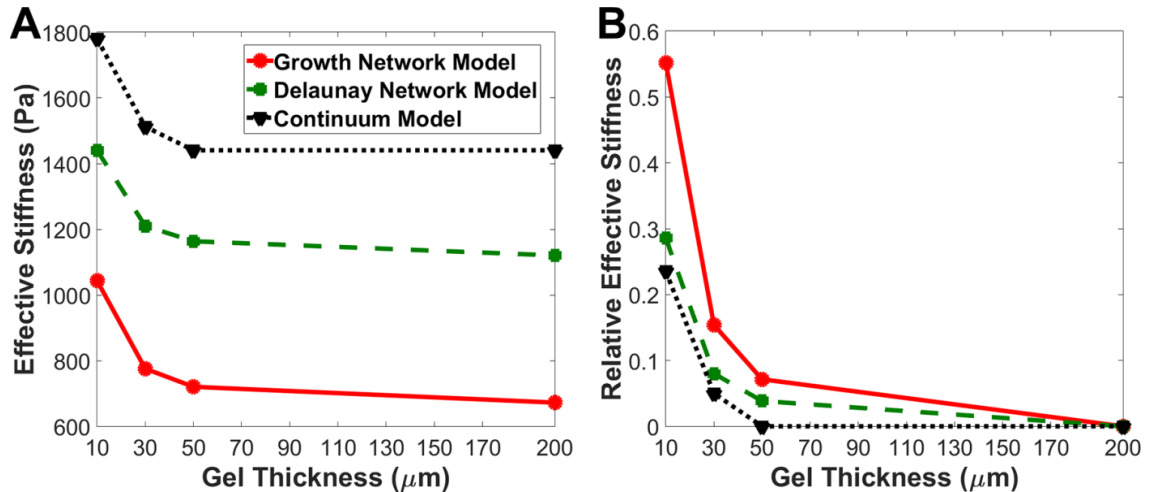
Figure 4-6: Comparison of (A) effective stiffness and (B) relative effective stiffness normalized to the 200 µm thick gel for each model.

50

www.manaraa.com

Comparison between Growth Network and Delaunay Network Fiber Models

The role of fiber network microstructure in the model was also assessed by comparing differences between *Growth Network Fiber* and *Delaunay Network Fiber* models. Even though the shear response of the *Delaunay Network* model closely followed the *Growth Network* model in approximating the experimental data, the model simulations produced noticeably different results in response to the applied cell traction force. The average principal stresses in the FA area (Table 4-2) were comparable to the *Growth Network* model (Figure 4-3B, Figure 4-4B) but mostly lower for the *Delaunay Network* model, particularly as the thickness increased. (Figure 4-3C, Figure 4-4C). The *Delaunay Network* model average nodal displacements, however, were nearly 1.5 times lower (Table 4-2). In addition, the effective stiffness of the *Delaunay Network* model was higher than the *Growth Network* model, but showed less sensitivity to an increase in gel thickness (Figure 4-6). Force propagation both laterally and into the depth of the gel was also much lower and less sensitive to an increase in gel thickness in the *Delaunay Network*. An assessment of this was made by arbitrarily locating the vertical distance at which nodal displacements dropped below 0.9 µm. For the *Growth Network* model, this vertical distance was approximately 5.0 µm, 17.5 µm, and 30.0 µm away from the focal adhesion area for gel thicknesses of 10 µm, 30 µm, and 50 µm, respectively. This distance was much less extensive in the *Delaunay Network* model, extending approximately 3.1 µm, 5.0 µm, and 5.0 µm for gel thicknesses of 10 µm, 30 µm, and 50 µm, respectively.

To further explore the basis for the greater sensitivity to substrate thickness observed in the *Growth Network* model, the accompanying changes in fiber microstructural reorganization in both *Fiber Network* models was also assessed. For both *Growth* and *Delaunay Network* models, networks that were initially nominally isotropic underwent a greater amount of realignment near where the traction forces were applied (i.e., the focal adhesion area) than networks farther away (Figure 4-7). The fiber realignment (α) and the magnitude of the change in fiber alignment with respect to the initial network configuration in the unloaded state ($\Delta\alpha$) also grew with increasing gel thickness and was much higher in the *Growth Network* model than in the *Delaunay Network* model. For example, if one considers the same block of 25 elements on the top surface and from the left surface to the outer edge of the cell for all thicknesses, the change in fiber alignment ($\Delta\alpha$) was 0.35 ± 0.10, 0.39 ± 0.06 and 0.40 ± 0.08 in the *Growth Network* model and 0.32 ± 0.16, 0.35 ± 0.16 and 0.36 ± 0.14 in the *Delaunay Network* model, for gel thicknesses of 10 µm, 30 µm, and 50 µm, respectively. The average strength of fiber alignment (α) also grew with increasing gel thickness and was higher in the *Growth Network* model, 0.50 ± 0.10, 0.53 ± 0.07 and 0.54 ± 0.07, than in the *Delaunay Network* model, 0.41 ± 0.17, 0.44 ± 0.15 and 0.44 ± 0.14, for gel thicknesses of 10 µm, 30 µm, and 50 µm, respectively. This pattern of enhanced network reorganization with increasing gel thickness seems to have occurred because the increasing distance of the rigid lower boundary from the gel surface reduced the constraints on fiber rotational freedom, which in turn facilitated more fiber alignment and the lower effective stiffnesses observed in thicker gels. This effect was likely more prominent in the *Growth Network* model because of the lower degree of connectivity

52

amongst the fibers in the network, which translated into less restrictions on fiber movement and greater displacements in the model compared to the more connected networks in the *Delaunay Network* model. In addition, finite elements which had networks with a change in network fiber alignment of $\Delta\alpha > 0.1$ were detected at vertical distances of approximately 10 µm, 30 µm, and 40 µm away from the focal adhesion area for gel thicknesses of 10 µm, 30 µm, and 50 µm, respectively. This propagation was again much less extensive in the *Delaunay Network* model, extending only as far as approximately 10 µm regardless of gel thickness.
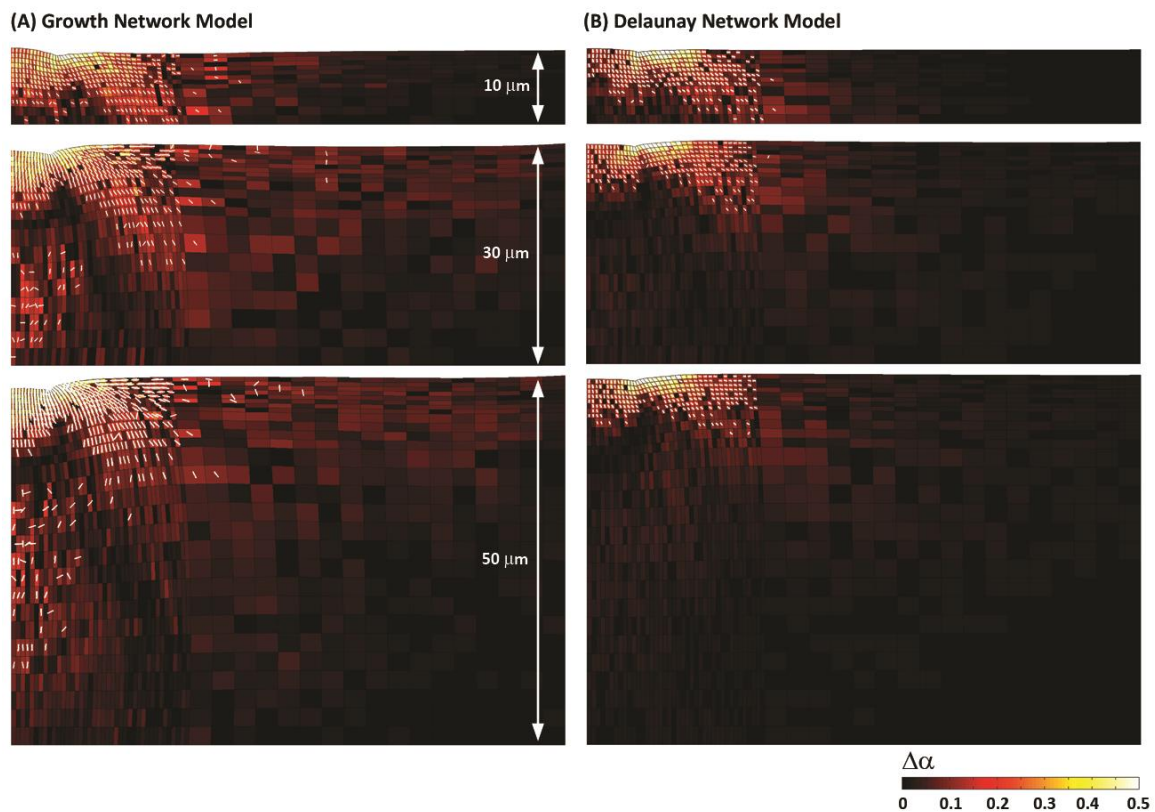
Figure 4-7: (A) *Growth Network* model, and (B) *Delaunay Network* model fiber network realignments for 10 µm, 30 µm, and 50 µm thick gels in response to 6 nN of traction force. The color map indicates the change in the degree of fiber alignment ($\Delta\alpha$) from the initial, nominally isotropic, traction free configuration. Also, depicted is the principal direction of fiber alignment (white lines). For clarity, principal directions are only shown for those elements with $\Delta\alpha > 0.1$.

A detailed view of how two networks in the 10 µm thick *Growth Network* model reorganized in response to the cell traction force is depicted in Figure 4-8. The first network (Figure 4-8A), which was located outside the focal adhesion area underneath the inner region of the cell, gradually elongated in the vertical direction while compressing laterally and rotating slightly to the right to produce a small shearing motion. At the conclusion of the simulation (i.e., Step 55), 75% of the fibers in this network were in tension (0.17 ± 0.32 nN) and 22% of the fibers were in compression (-0.16 ± 0.37 nN). Combined, these tensile and compressive forces corresponded to an average network fiber force of 0.10 ± 0.35 nN (maximum and minimum fiber forces of 2.01 nN and -2.14 nN, respectively). A second network (Figure 4-8B), located directly under and inside the inner boundary of the focal adhesion area, experienced a much larger shearing motion with fibers aligning diagonally toward the direction of the applied force. At Step 55, 78% of the fibers were in tension (0.42 ± 0.55 nN) and 21% were in compression (-0.22 ± 0.39 nN), which corresponded to an average fiber force of 0.28 ± 0.59 nN (maximum and minimum fiber forces of 2.57 nN and -2.57 nN, respectively).
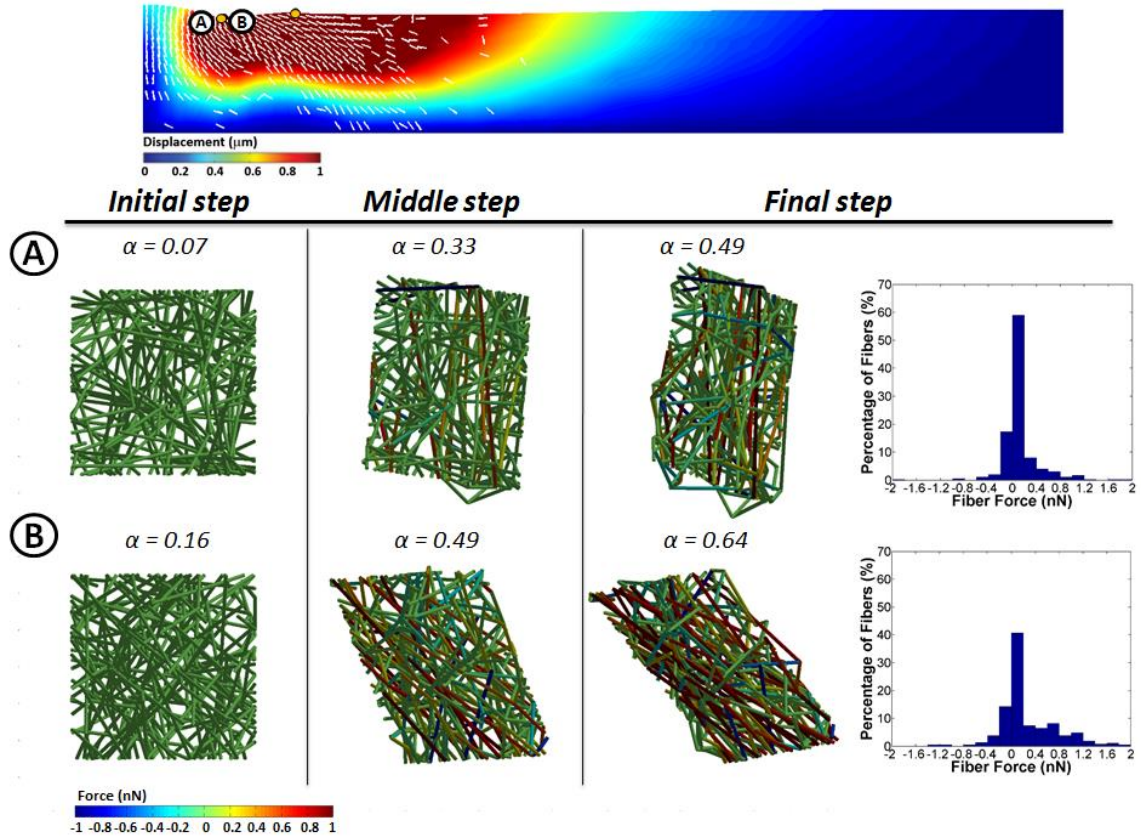
Figure 4-8: *Growth* fiber network behavior at selected locations. The direction of fiber alignment is shown on the 10 µm case displacement field for $\Delta\alpha > 0.1$, the orange circles indicate the inner and outer boundaries of the focal adhesion area, and the lettered white circles indicate the locations of networks A and B shown below. Network organization, fiber forces, and fiber anisotropy index are shown for the initial, middle, and final steps of the simulation. Fiber force histograms are also shown for the final step of the simulation.

Differences in *Delaunay Network* reorganization were also evident. Changes in network shape and volume were slightly less pronounced, and a higher fraction of fibers were in compression than tension For example, 54% (Figure 4-9A) and 49% (Figure 4-9B) of the fibers in networks at equivalent locations as in the *Growth Network* model were in compression at Step 55. As a result, the average fiber forces in the network were -0.05 ± 0.35 nN (maximum and minimum fiber forces of 0.88 nN and -0.81 nN, respectively) and 0.10 ± 0.60 nN (maximum and minimum fiber forces of 2.20 nN and -0.96 nN, respectively) for networks A and B, respectively. The change in the strength of

fiber alignment (Δα) at step 55 was comparable but lower in the *Delaunay Network* model (0.34 and 0.47) than in the *Growth Network* model (0.42 and 0.48) for networks A and B, respectively.
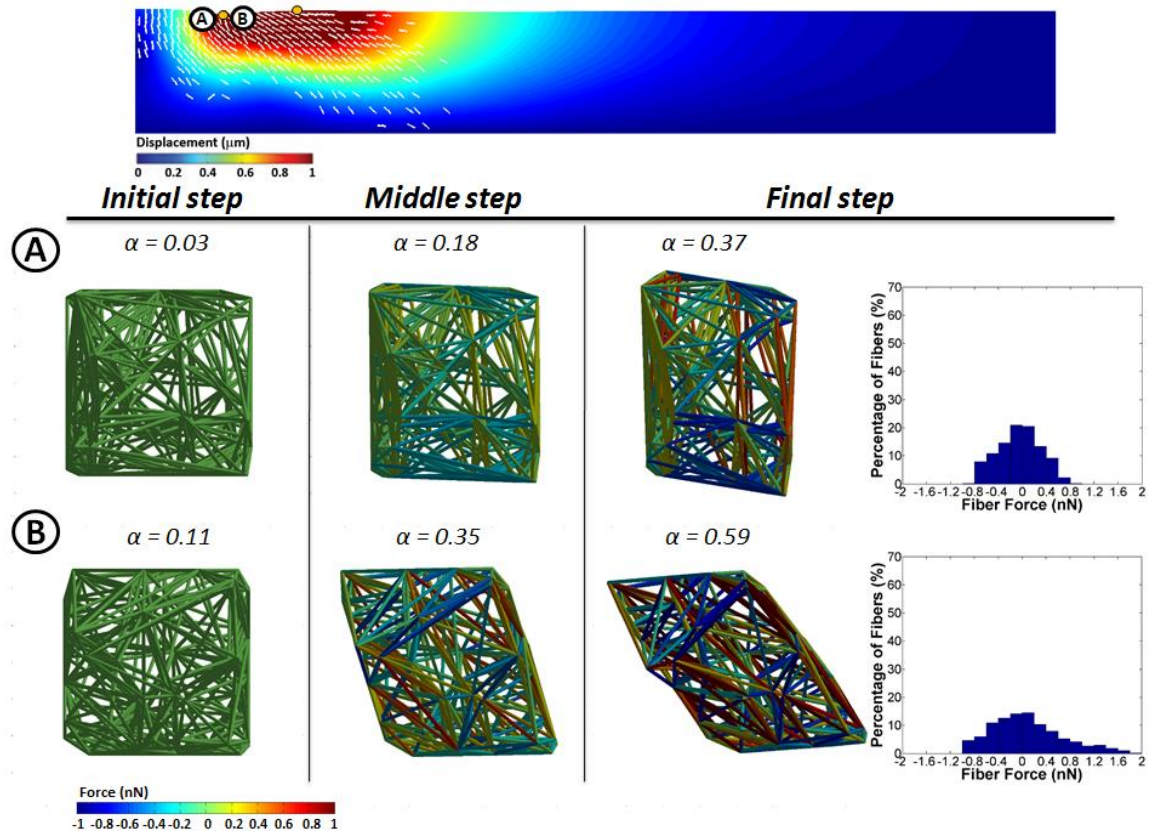
Figure 4-9: *Delaunay* fiber network behavior at selected locations. The direction of fiber alignment is shown on the 10 µm case displacement field for $\Delta\alpha > 0.1$, the orange circles indicate the inner and outer boundaries of the focal adhesion area, and the lettered white circles indicate the locations of networks A and B. Network organization, fiber forces, and fiber anisotropy index are shown for the initial, middle, and final steps of the simulation. Fiber force histograms are also shown for the final step.

4.4 Discussion

In conducting this comprehensive comparison of model differences between non-linear continuum and fiber-based FE models, we found that (1) the *Growth Network* model predicted much larger displacements both laterally and through the depth than the

Continuum model for the same amount of traction force due to the ability of the fibers to rotate and stretch, and that (2) the representation of the network was critically important, particularly with respect to fiber connectivity. The low fiber connectivity in the *Growth Network* model fostered greater fiber realignment and displacement propagation into the gel with a greater sensitivity to the gel thickness than in the highly connected *Delaunay Network* model. The *Delaunay Network* model exhibited reduced displacement propagation, fiber realignment, and thickness sensitivity such that these model predictions approached those of the non-linear continuum model. These results highlight the importance of fiber connectivity and its role in extending the distance that mechanical information is transmitted from the boundaries, which could have implications for the design of engineered soft tissues and stem cell niches.

To facilitate model comparisons, the material parameters for all three models were selected so that the model response to shear matched a fibrin gel shear test. Even though this mode of shear deformation most closely resembled that of the applied cell traction force, other modes of deformation (as well as small differences in how each model matched the mechanical response) likely contributed to the differences in the mechanical responses observed amongst the models, particularly with respect to the non-normalized effective stiffness. Because the applied traction force and model geometry was equivalent in each model, the effective stiffness was only dependent on the inverse of the mean displacements in the FA area. These displacements were small in all models, but the differences were large enough that the non-normalized effective stiffness for the *Growth Network* model was much lower than for the other two models. These results, together with the larger displacement propagation distances in both the vertical and

57

horizontal directions, indicate that the *Growth Network* model was locally "softer" than the other two models even though all three models have comparable bulk material properties in shear.

Because the effective stiffness values are based on relatively small displacements, the differences between models could also reflect how well each model fit the experimental shear data. To check for this possibility, we also chose to calculate metrics based on the sensitivity of each individual model to an increase in gel thickness. Consistent with our previous work (12), we calculated the normalized effective stiffness with respect to a semi-infinite gel, approximated here by the values obtained for a 200 µm thick gel. The normalized effective stiffness also indicates that the *Growth Network* model was much more sensitive to changes in gel thickness than the other two models (Figure 4-6B). This increased sensitivity is reflected in the observation that there was still a small increase in the mean displacement in the FA area of 7.1% between the 50 µm and 200 µm gels for the *Growth Network* model, but there was only a 3.8% increase for the *Delaunay Network* model and no change for the *Continuum* model over the same span of gel thicknesses. This result can be interpreted to mean that the depth at which the rigid boundary still has some influence was much greater for the *Growth Network* model. We also calculated the critical gel thickness, h_{crit}, and saturation maximum displacement, u_{inf}, for each model (Table 4-3) according to the equation used by us previously (12) and given per Sen *et al.* (20): $u_{max} = (h \times u_{inf})/(h + h_{crit})$, where u_{max} is the maximum surface displacement and h is the gel thickness. h_{crit} represents the gel thickness at which the maximum surface displacement reaches half of the value obtained for a gel of semi-infinite thickness and u_{inf} is the saturation displacement reached on a semi-infinite gel.

Both u_{inf} and h_{crit} were much higher for the *Growth Networks*, which also supports the notion that mechanical communication and depth sensitivity is enhanced in the *Growth Networks*.

Table 4-3: Fit parameters for critical thickness, h_{crit}, and saturation maximum surface displacement, u_{inf}, for each model.

Model	u_{inf} [µm]	h_{crit} [µm]
Continuum	2.27	1.66
Delaunay Network	2.85	2.45
Growth Network	4.82	5.39

The traction forces applied to the gel are shared between the gel and the rigid underlying substrate in a manner that is dependent on the thickness of the gel (86). As the gels get thicker, a saturation thickness is reached at which the rigid substrate no longer has an influence on the mechanical response to the applied tractions, and all of the applied load is carried by the gel (i.e., the gel can be considered semi-infinite). We consider this saturation thickness as representative of the cell's maximum possible depth sensing distance for a given traction force. The introduction of fibers into the model extended this distance compared to a non-linear continuum model, particularly with respect to the *Growth Networks*, which due to their low degree of fiber connectivity, had fibers with greater rotational freedom. As the distance of the rigid lower boundary increased, the fibers in the networks experienced greater realignment towards the lower boundary compared to the more connected (and therefore more constrained) fibers in the *Delaunay Network* model. This had the two-fold effect of making the *Growth Network*

59

model appear softer locally and of extending the depth of fiber realignment and force propagation.

The results from this study support the growing body of experimental and theoretical work that indicates that the fibrous nature of biological gels is responsible for enhanced long-distance cell mechanosensing compared to non-fibrous gels (12-15, 87-90). Several of these theoretical studies have found that the mechanosensing length scale of a cell increases when fibers are accounted for in the model (12, 87, 89, 90). For example, Ma *et al*. developed an image-based 2D FE model of two cells separated by a distance of ~100 µm and surrounded by a network of linear elastic collagen fibers embedded in a soft nonfibrous material with mechanical properties selected from the literature (87). This model also found that forces were only transmitted long distances from one contracting cell to the other when the fibers were explicitly accounted for due to improved force transmission along aligned fibers. If the surrounding material was represented instead by a homogeneous non-linear strain-hardening material, then the stresses rapidly decayed a short distance away from the cells and no mechanical communication occurred between the two cells. Another key property of the networks that facilitates fiber alignment and the transmission of long-range mechanical signals is the low compressive resistance of the fibers (relative to the tensile stiffness), which Notbohm *et al*. also reported and referred to as microbuckling (90). In this context, microbuckling does not refer to a mechanism of failure, but instead means that less energy is needed for fibers in the network to compress in order to accommodate the realignment of other network fibers in tension. In our simulations, even with microbuckling, a highly connected network, such as the *Delaunay Network*, exhibited reduced depth sensing compared to network with low

60

connectivity (i.e., *Growth Network*) because the ability of fibers to rotate and realign was reduced. Thus, from our point of view, those network properties that facilitate fiber reorientation (i.e., low fiber connectivity, microbuckling, rotational freedom at the crosslinks) work together to enhance long-range force transmission.

The mechanics of fiber networks are dependent on a number of network properties, such as the density of fibers and crosslinks, the distribution of fiber lengths and fiber orientations, the fiber connectivity (number of fibers connecting at a crosslink), and the nature of the crosslinks (e.g. a freely rotating ball joint or a fixed joint). Exploration of all of these complex relationships was beyond the scope of this study and are reviewed elsewhere (69, 91). Instead, we chose to limit our analysis to two fundamentally different types of networks that primarily differ in the number of fibers connected by a crosslink (i.e., connectivity), and that we believe are reasonable idealizations of network structure one might find for substrates used in mechanobiological studies. We have used the less connected *Growth Network* to successfully represent the low fiber connectivity typically found in dilute collagen and fibrin gels (85, 92-94). The more highly connected *Delaunay Networks* represent a shift up the connectivity spectrum towards the limiting case of a fully connected and continuous material. In addition, the *Delaunay Networks* are likely more representative of synthetic polymers and other highly crosslinked hydrogels that resemble cellular solids (95) and that could be used as cell substrates either for mechanobiological studies or regenerative medicine applications. Thus, both types of networks should be useful for understanding in vitro experimental findings on cell responses on different materials. Finally, cell tractions were simulated as a constant force equally distributed amongst the nodes of the

61

focal adhesion area. However, cells likely adjust the tractions they exert on the substrate as part of a feedback loop in order to achieve some set point of baseline tension. Such mechanisms have been included in other modeling schemes (78, 89), and future work will seek to incorporate such cell feedback into this model.

In conclusion, traction forces produce a greater propagation of displacements through *Growth Networks* than through more connected *Delaunay Networks* and continuum models. Rotational freedom of the fibers in an extracellular matrix network with low fiber connectivity appear to be critical for the enhanced, long-range mechanosensing observed experimentally for cells cultured on fibrous gels. These results aid our understanding of cell-cell communication within sparse tissues and have implications for the design of engineered soft tissue replacements.

CHAPTER 5

A DISCRETE MECHANISTIC NETWORK-BASED MODELING OF CELL

MIGRATION, AND COUPLING IT TO A SUBSTRATE MODEL

5.1 Introduction

The purpose of this chapter is to develop a computational model that accounts for active cellular component to help understand the dynamics and reciprocal nature of the cell's mechanical environment. We develop a type of two-dimensional agent-based model that is a mechanistic network representation of mechanosensing cells. This model is coupled to a three-dimensional representation of the substrate. The active cell model is based primarily on physical and conservation laws and represents cells as mechanical elements that interact with each other and the extracellular matrix (ECM).

5.2 Methods

The incorporation of individual, autonomous cells that can migrate and interact with other cells and the ECM based on a set of rules that provide positive and negative mechanical feedback is important in representation of cells. To begin to address these issues, we develop a type of cell model, which is then coupled to a substrate model. The model is based primarily on physical and conservation laws rather than a collection of conditional if then statements that are difficult to pin down to physical mechanisms. We choose this approach because network models have been used successfully to describe mechanical feedback between cells and substrates.

63

5.2.1 Cell Biomechanics and Migration

Cell that is represented by a two-dimensional Delaunay network is constructed and force-based rules similar to the model proposed by Dokukina *et al*. is utilized (30). The network, which represents the cell cytoskeleton coarsely, consists of nodes that are connected together by elastic springs and viscous dashpots in parallel (Figure 5-1). When the resting lengths between the nodes changes, cytoskeletal viscoelastic forces, $\vec{F}_i^{Viscoelastic}$, are developed. Active forces, $\vec{F}_i^{Active}$, are applied to defined nodes at the front of the cell in order to simulate the propulsive forces generated from actin polymerization at the leading edge of the lamellipodium. Cell adhesions to the extracellular matrix (ECM) will be approximated as a drag force, $\vec{F}_i^{Drag}$, so that a cell velocity can be calculated. These forces must balance at each node i in the network according to:

$$\vec{F}_i^{Drag} + \vec{F}_i^{Viscoelastic} = \vec{F}_i^{Active} \tag{5.1}$$

which can be expanded to:

$$\mu_{0i}\frac{\partial \vec{r}_i}{\partial t} + \sum_{j=1}^{M_i}\left(\mu\frac{\partial \varepsilon_{ij}}{\partial t} + E_{ij}\varepsilon_{ij}\right)\hat{r}_{ij} = \vec{F}_i^{Active} \tag{5.2}$$

where μ_{0i} is the viscous drag coefficient for node i due to the cell-substrate interaction, $\vec{r}_i = (x_i, y_i)$ is the position vector of node i, E_{ij} is the cell cytoskeleton elasticity coefficient, μ is the cell cytoskeleton viscosity coefficient, ε_{ij} is the change in length between nodes i and j, and $\vec{r}_{ij}$ is the unit vector along the line connecting nodes i and j.

64
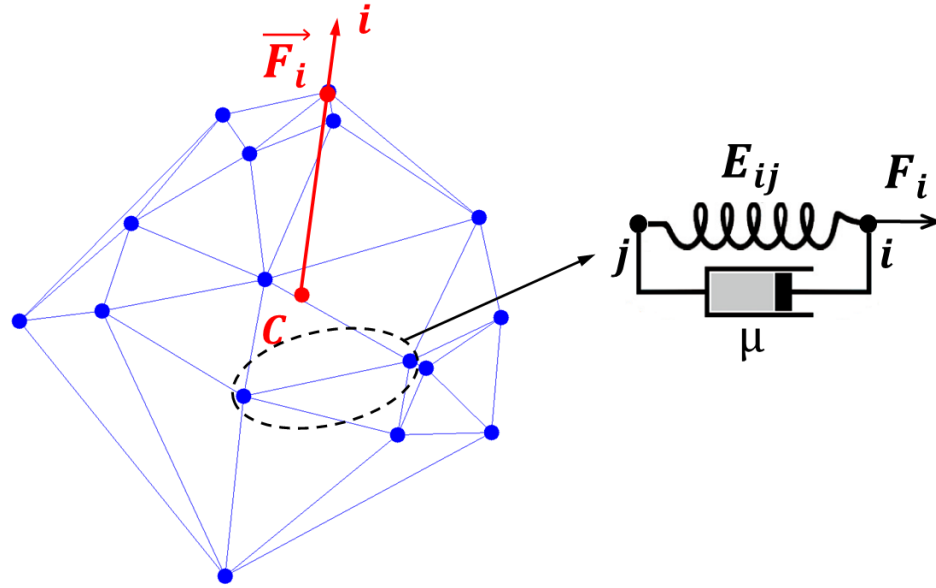
Figure 5-1: Two-dimensional Delaunay network representing cell, and the cytoskeleton mechanical properties. Neighboring nodes *i* and *j* are connected by elastic spring with elasticity coefficient E_{ij} and viscous dashpot with viscosity coefficient μ, in parallel. The active forces F_i are applied at the front of the cell. A representative force is marked by an arrow. The cell center is indicated by *C*.

5.2.1.1 Cell Viscoelasticity

The cytoskeletal modulus will decrease quadraticly from the front to the back of the cell in order to simulate experimentally observed spatial differences in cytoskeletal stiffness:

$$E_{ij} = E_{min} + (E_{max} - E_{min})\frac{(y_{ave} - y_{min})^2}{L_{cell}^2} \tag{5.3}$$

where $y_{ave} = \left(y_i(t=0) + y_j(t=0)\right)/2$ and $L_{cell} = y_{max}(t=0) - y_{min}(t=0)$ is the initial cell length. It is assumed that the elasticity coefficient is not dependent on the direction normal to the cell axis. The modulus values are assigned at the initial time and remain fixed thereafter.

5.2.1.2 Cell Matrix Interactions and Force Generation

The adhesion drag force is described by a viscosity coefficient multiplied by the cell speed. It is assumed that the viscosity coefficient, μ_{0i}, due to the cell substrate interaction at the ith node is a linearly increasing function of substrate rigidity:

$$\mu_{0i} = k \times \sigma_{ST}(x_i, y_i) \tag{5.4}$$

where k is the proportionality coefficient, and

$$\sigma_{ST} = \sigma_{min} - (\sigma_{min} - \sigma_{max})\frac{y^n}{y^n + L_b^n} \tag{5.5}$$

is the substrate rigidity at the ith node with coordinates (x_i, y_i).

Due to experimental observations that cells are able to develop stronger mechanical forces on stiffer substrates than on softer substrates, it is assumed that the active force generated by the cell increases with substrate rigidity (6). A Hill function is used here for the limited growth of active force with substrate rigidity. Therefore, the magnitude of the cell-generated force at ith front node is described as:

$$\left|F_i^{Active}\right| = \frac{|F_{Act}|}{N_{Front}} \times \frac{\sigma_{ST}^2}{\sigma_{ST}^2 + \sigma_{ave}^2} \tag{5.6}$$

Because of the presence of the position-dependent spring deformation ε_{ij} in the second time-derivative term, the force balance equations are nonlinear in node coordinates. Therefore, they were discretized and solved using a nonlinear iterative method at each time step (Appendix B).

66

5.2.2. Coupling Between Cell Migration and Substrate Models

The two-dimensional cell migration model, which has been developed, is coupled to the top surface of a three-dimensional substrate model, described by the compressible formulation of the neo-Hookean constitutive equation given as

$$\sigma_{ij}^{nH} = \frac{G}{J}\left(B_{ij} - \delta_{ij}\right) + \frac{2G\nu}{J\left(1-2\nu\right)}\left(\ln\left(J\right)\right)\delta_{ij} \tag{5.7}$$

where σ_{ij}^{nH} represents the compressible neo-Hookean stress (73), G is the shear modulus, ν is Poisson's ratio, J is the determinant of the deformation tensor, and B is the left Cauchy-Green deformation tensor.

The two-dimensional cell cytoskeleton is modeled by 16 nodes connected according to the Delaunay triangulation on the xy-plane and on the top surface of the three-dimensional substrate model represented by a square finite element mesh containing 20 elements along the length, 20 elements along the width, and one element through the depth and consisting of 400 tri-linear hexahedral elements and 882 nodes (Figure 5-2).

To simulate the cell migration coupled to the substrate model, all finite element mesh surfaces except the top surface, which remains free, are fixed.

We have already implemented nodal force boundary conditions in the finite element model to assess how far forces are transmitted through the substrate in chapter 4.

Cell cytoskeletal viscoelastic forces are interpolated and applied to substrate finite element mesh as traction forces. Substrate displacements are then calculated and interpolated to find the effective stiffness in a manner analogous to equation (4.4) utilized to update the cell viscous drag coefficient instead of using equation (5.5), and the

67

magnitude of the cell-generated force described by equation (5.6). Therefore, active cellular component is added to our model to understand how the cell dynamically and reciprocally interacts with the mechanical environment.
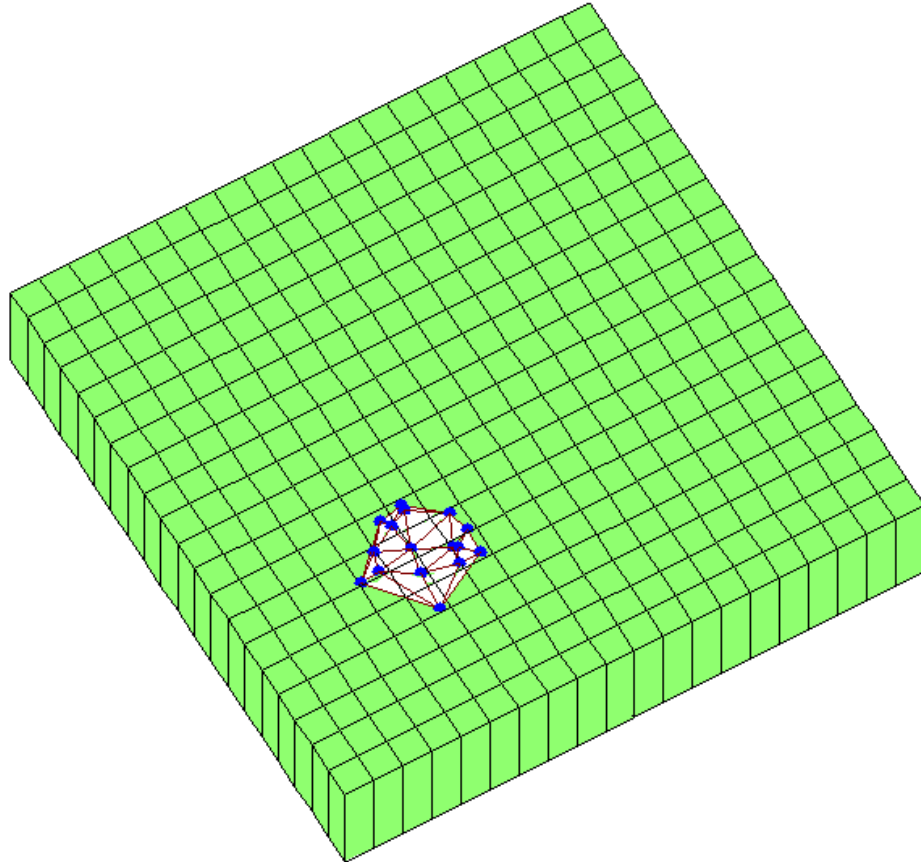
Figure 5-2: Schematic of the two-dimensional cell model on top surface of the three-dimensional finite element model. Cell traction forces are interpolated and applied to the finite element nodes on the top surface.

5.3 Results

First, we simulate cell motion from a softer side of substrate to a stiffer side of substrate (Figure 5-3). Cell, which is initially planted on the soft side of substrate and has a cell-generated force applied to the 3 front nodes, migrates from the soft to the stiff side.

The model cell migrating to the stiff side of the substrate, stretches and its projected area increases.
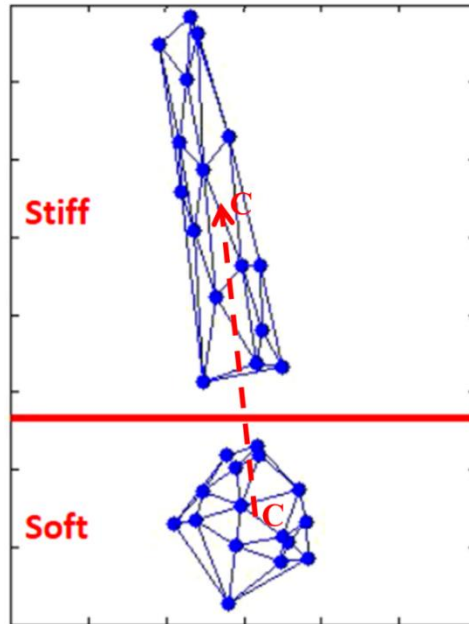
Figure 5-3: The cell moves from the soft side of the substrate toward the stiff side of the substrate. The trajectory of the cell center is marked with a dashed arrow.

The cell migration model coupled to the substrate model is presented in Figure 5-4 at initial, middle and final steps. Cell traction forces calculated from the cell model are interpolated and applied to the finite element mesh causing the substrate to deform, which in turn change the effective stiffness of the underlying matrix and the cell-generated force, and affect the force balances on the cell network nodes, the cell shape and the direction of movement.
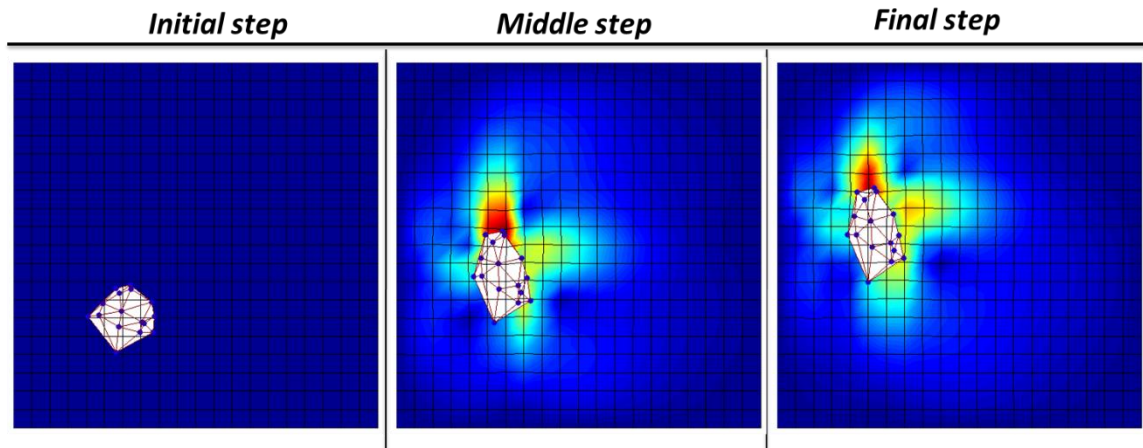
Figure 5-4: Displacement fields for the cell migration model coupled to the substrate model at initial, middle and final steps.
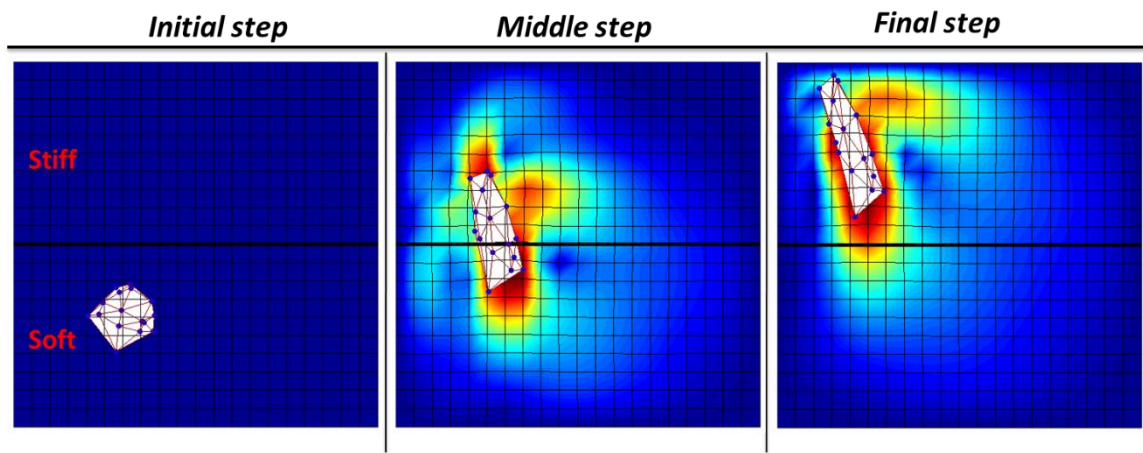
Figure 5-5: Displacement fields for the cell migration coupled to the substrate with a step in stiffness at initial, middle and final steps.

The cell migration model coupled to the substrate model with a step in stiffness is presented in Figure 5-5 at initial, middle and final steps. The cell at the same initial location on the substrate with the same stiffness and with the same initial force generated at the front nodes and the same total migration time as the cell in Figure 5-4, readily

moves towards and crosses the boundary with the substrate that is three times stiffer, in a manner similar to the experimental observations (6).

Compared with the cells on soft substrates, those on stiff substrates showed increased spreading area (6, 9). The cell area moving from the soft side to the stiff side of the substrate increased about 33% and 38% of the initial cell area, at the middle and final steps, respectively, whereas, the cell remaining on the soft substrate had a less increase in area (about 20% of the initial area at both the middle and final steps). Furthermore, the cell average speed and migration distance for the cell moving from the soft side to the stiff side of the substrate was higher (more than 2 times) than for the cell remaining on the soft substrate, which was also consistent with experiments (6).

The maximum substrate displacements for the cell moving from the soft side to the stiff side of the substrate was happening at cell rear that was on the soft side or close to the soft side of the substrate and was larger (about 18% and 16% at the middle and final steps, respectively) than for the cell remaining on the soft substrate, which had the maximum substrate displacements occurring at the cell front. This is because of increasing the cell-generated force at the front nodes with the substrate rigidity and effective stiffness and the lower force on the softer substrate in the model, which was also observed experimentally (6).

5.4 Discussion

Computational models that account for active cellular component to help understand the dynamics and reciprocal nature of the cell's mechanical environment observed experimentally, are developed.

71

Cell prefers migrating towards and over the stiffer substrate than the softer substrate. The cell model qualitatively describes experimental observations, and substrate rigidity sensing, which allows us to gain additional insights into the cell mechanosensitivity.

Coupling between the cell migration and the substrate models adds a new feedback mechanism as cell traction forces on the substrate cause the finite element mesh to deform, which in turn change the effective stiffness of the underlying matrix, and affect the cell forces, shape, spread area, speed and direction of motility.

The simulations are performed in MATLAB. This model can also be implemented in a three-dimensional fiber-based representation of the substrate in a parallelized C code.

REFERENCES

1.   Yip CYY, Chen JH, Zhao RG, Simmons CA. Calcification by Valve Interstitial Cells Is Regulated by the Stiffness of the Extracellular Matrix. Arterioscl Throm Vas. 2009;29(6):936-U417.

2.   Saha K, Keung AJ, Irwin EF, Li Y, Little L, Schaffer DV, et al. Substrate modulus directs neural stem cell behavior. Biophysical journal. 2008;95(9):4426-38.

3.   Discher DE, Janmey P, Wang YL. Tissue cells feel and respond to the stiffness of their substrate. Science. 2005;310(5751):1139-43.

4.   Lutolf MP, Gilbert PM, Blau HM. Designing materials to direct stem-cell fate. Nature. 2009;462(7272):433-41.

5.   Reilly GC, Engler AJ. Intrinsic extracellular matrix properties regulate stem cell differentiation. J Biomech. 2010;43(1):55-62.

6.   Lo CM, Wang HB, Dembo M, Wang YL. Cell movement is guided by the rigidity of the substrate. Biophys J. 2000;79(1):144-52.

7.   Guilak F, Butler DL, Goldstein SA, Baaijens FP. Biomechanics and mechanobiology in functional tissue engineering. J Biomech. 2014;47(9):1933-40.

8.   De Jesus AM, Aghvami M, Sander EA. A Combined In Vitro Imaging and Multi-Scale Modeling System for Studying the Role of Cell Matrix Interactions in Cutaneous Wound Healing. PLoS One. 2016;11(2):e0148254.

9.   Pelham RJ, Jr., Wang Y. Cell locomotion and focal adhesions are regulated by substrate flexibility. Proc Natl Acad Sci U S A. 1997;94(25):13661-5.

10.   Evans ND, Minelli C, Gentleman E, LaPointe V, Patankar SN, Kallivretaki M, et al. Substrate stiffness affects early differentiation events in embryonic stem cells. Eur Cell Mater. 2009;18:1-13; discussion -4.

11.   Engler AJ, Sen S, Sweeney HL, Discher DE. Matrix elasticity directs stem cell lineage specification. Cell. 2006;126(4):677-89.

12.   Rudnicki MS, Cirka HA, Aghvami M, Sander EA, Wen Q, Billiar KL. Nonlinear strain stiffening is not sufficient to explain how far cells can feel on fibrous protein gels. Biophys J. 2013;105(1):11-20.

13.   Winer JP, Oake S, Janmey PA. Non-linear elasticity of extracellular matrices enables contractile cells to communicate local position and orientation. PLoS One. 2009;4(7):e6382.

14.   Leong WS, Tay CY, Yu H, Li A, Wu SC, Duc DH, et al. Thickness sensing of hMSCs on collagen gel directs stem cell fate. Biochem Biophys Res Commun. 2010;401(2):287-92.

15.   Ali MY, Chuang CY, Saif MT. Reprogramming cellular phenotype by soft collagen gels. Soft Matter. 2014;10(44):8829-37.

16.   Breuls RG, Sengers BG, Oomens CW, Bouten CV, Baaijens FP. Predicting local cell deformations in engineered tissue constructs: a multilevel finite element approach. J Biomech Eng. 2002;124(2):198-207.

17.   Guilak F, Mow VC. The mechanical environment of the chondrocyte: a biphasic finite element model of cell-matrix interactions in articular cartilage. J Biomech. 2000;33(12):1663-73.

18. Susilo ME, Bell BJ, Roeder BA, Voytik-Harbin SL, Kokini K, Nauman EA. Prediction of equibiaxial loading stress in collagen-based extracellular matrix using a three-dimensional unit cell model. Acta Biomater. 2013;9(3):5544-53.

19. Corin KA, Gibson LJ. Cell contraction forces in scaffolds with varying pore size and cell density. Biomaterials. 2010;31(18):4835-45.

20. Sen S, Engler AJ, Discher DE. Matrix strains induced by cells: Computing how far cells can feel. Cell Mol Bioeng. 2009;2(1):39-48.

21. Mehrotra S, Hunley SC, Pawelec KM, Zhang L, Lee I, Baek S, et al. Cell adhesive behavior on thin polyelectrolyte multilayers: cells attempt to achieve homeostasis of its adhesion energy. Langmuir. 2010;26(15):12794-802.

22. Notbohm J, Lesman A, Rosakis P, Tirrell DA, Ravichandran G. Microbuckling of fibrin provides a mechanism for cell mechanosensing. J R Soc Interface. 2015;12(108):20150320.

23. Abhilash AS, Baker BM, Trappmann B, Chen CS, Shenoy VB. Remodeling of fibrous extracellular matrices by contractile cells: predictions from discrete fiber network simulations. Biophys J. 2014;107(8):1829-40.

24. Janmey PA, Miller RT. Mechanisms of mechanical signaling in development and disease. J Cell Sci. 2011;124(Pt 1):9-18.

25. Pedersen JA, Swartz MA. Mechanobiology in the third dimension. Ann Biomed Eng. 2005;33(11):1469-90.

26. Geiger B, Spatz JP, Bershadsky AD. Environmental sensing through focal adhesions. Nat Rev Mol Cell Biol. 2009;10(1):21-33.

27. Sander EA, Barocas VH, Tranquillo RT. Initial fiber alignment pattern alters extracellular matrix synthesis in fibroblast-populated fibrin gel cruciforms and correlates with predicted tension. Ann Biomed Eng. 2011;39(2):714-29.

28. Aarabi S, Bhatt KA, Shi Y, Paterno J, Chang EI, Loh SA, et al. Mechanical load initiates hypertrophic scar formation through decreased cellular apoptosis. FASEB J. 2007;21(12):3250-61.

29. Schluter DK, Ramis-Conde I, Chaplain MA. Computational modeling of single-cell migration: the leading role of extracellular matrix fibers. Biophys J. 2012;103(6):1141-51.

30. Dokukina IV, Gracheva ME. A model of fibroblast motility on substrates with different rigidities. Biophys J. 2010;98(12):2794-803.

31. Reinhardt JW, Krakauer DA, Gooch KJ. Complex matrix remodeling and durotaxis can emerge from simple rules for cell-matrix interaction in agent-based models. J Biomech Eng. 2013;135(7):71003.

32. Marinkovic A, Mih JD, Park JA, Liu F, Tschumperlin DJ. Improved throughput traction microscopy reveals pivotal role for matrix stiffness in fibroblast contractility and TGF-beta responsiveness. Am J Physiol Lung Cell Mol Physiol. 2012;303(3):L169-80.

33. Sieminski AL, Hebbel RP, Gooch KJ. The relative magnitudes of endothelial force generation and matrix stiffness modulate capillary morphogenesis in vitro. Exp Cell Res. 2004;297(2):574-84.

34. Wells RG. The role of matrix stiffness in hepatic stellate cell activation and liver fibrosis. J Clin Gastroenterol. 2005;39(4 Suppl 2):S158-61.

35. Schwartz MA, DeSimone DW. Cell adhesion receptors in mechanotransduction. Curr Opin Cell Biol. 2008;20(5):551-6.

36.   Wozniak MA, Modzelewska K, Kwong L, Keely PJ. Focal adhesion regulation of cell behavior. Biochim Biophys Acta. 2004;1692(2-3):103-19.

37.   Genin GM, Abney TM, Wakatsuki T, Elson EL. Cell-Cell Interactions and the Mechanics of Cells and Tissues Observed in Bioartificial Tissue Constructs. Mechanobiology of Cell-Cell and Cell-Matrix Interactions: Springer; 2011. p. 75-103.

38.   Peacock M, Turner CH, Econs MJ, Foroud T. Genetics of osteoporosis. Endocr Rev. 2002;23(3):303-26.

39.   Rubin CT, Lanyon LE. Osteoregulatory nature of mechanical stimuli: function as a determinant for adaptive remodeling in bone. Journal of Orthopaedic Research. 1987;5(2):300-10.

40.   Burgoyne CF, Downs JC, Bellezza AJ, Suh J-KF, Hart RT. The optic nerve head as a biomechanical structure: a new paradigm for understanding the role of IOP-related stress and strain in the pathophysiology of glaucomatous optic nerve head damage. Progress in retinal and eye research. 2005;24(1):39-73.

41.   Sander EA, Downs JC, Hart RT, Burgoyne CF, Nauman EA. A cellular solid model of the lamina cribrosa: mechanical dependence on morphology. J Biomech Eng. 2006;128(6):879-89.

42.   Moore JE, Jr., Xu C, Glagov S, Zarins CK, Ku DN. Fluid wall shear stress measurements in a model of the human abdominal aorta: oscillatory behavior and relationship to atherosclerosis. Atherosclerosis. 1994;110(2):225-40.

43.   Nerem RM. Vascular fluid mechanics, the arterial wall, and atherosclerosis. J Biomech Eng. 1992;114(3):274-82.

44.   Gao L, Hoi Y, Swartz DD, Kolega J, Siddiqui A, Meng H. Nascent aneurysm formation at the basilar terminus induced by hemodynamics. Stroke. 2008;39(7):2085-90.

45.   Paszek MJ, Zahir N, Johnson KR, Lakins JN, Rozenberg GI, Gefen A, et al. Tensional homeostasis and the malignant phenotype. Cancer Cell. 2005;8(3):241-54.

46.   Huang S, Ingber DE. Cell tension, matrix mechanics, and cancer development. Cancer Cell. 2005;8(3):175-6.

47.   Pathak A, Kumar S. Independent regulation of tumor cell migration by matrix stiffness and confinement. Proc Natl Acad Sci U S A. 2012;109(26):10334-9.

48.   Balestrini JL, Billiar KL. Magnitude and duration of stretch modulate fibroblast remodeling. J Biomech Eng. 2009;131(5):051005.

49.   Rubbens MP, Driessen-Mol A, Boerboom RA, Koppert MM, van Assen HC, TerHaar Romeny BM, et al. Quantification of the temporal evolution of collagen orientation in mechanically conditioned engineered cardiovascular tissues. Ann Biomed Eng. 2009;37(7):1263-72.

50.   Seliktar D, Black RA, Vito RP, Nerem RM. Dynamic mechanical conditioning of collagen-gel blood vessel constructs induces remodeling in vitro. Ann Biomed Eng. 2000;28(4):351-62.

51.   Juncosa-Melvin N, Matlin KS, Holdcraft RW, Nirmalanandhan VS, Butler DL. Mechanical stimulation increases collagen type I and collagen type III gene expression of stem cell-collagen sponge constructs for patellar tendon repair. Tissue Eng. 2007;13(6):1219-26.

52.   Brown RA, Prajapati R, McGrouther DA, Yannas IV, Eastwood M. Tensional homeostasis in dermal fibroblasts: mechanical responses to mechanical loading in three-dimensional substrates. J Cell Physiol. 1998;175(3):323-32.

53.   Syedain ZH, Weinberg JS, Tranquillo RT. Cyclic distension of fibrin-based tissue constructs: evidence of adaptation during growth of engineered connective tissue. Proc Natl Acad Sci U S A. 2008;105(18):6537-42.

54.   Aghvami M, Barocas VH, Sander EA. Multiscale mechanical simulations of cell compacted collagen gels. J Biomech Eng. 2013;135(7):71004.

55.   Stylianopoulos T, Barocas VH. Volume-averaging theory for the study of the mechanics of collagen networks. Computer methods in applied mechanics and engineering. 2007;196(31):2981-90.

56.   Sander EA, Stylianopoulos T, Tranquillo RT, Barocas VH. Image-based biomechanics of collagen-based tissue equivalents. IEEE Eng Med Biol Mag. 2009;28(3):10-8.

57.   Chandran PL, Barocas VH. Affine versus non-affine fibril kinematics in collagen networks: theoretical studies of network behavior. J Biomech Eng. 2006;128(2):259-70.

58.   Stylianopoulos T, Bashur CA, Goldstein AS, Guelcher SA, Barocas VH. Computational predictions of the tensile properties of electrospun fibre meshes: effect of fibre diameter and fibre orientation. J Mech Behav Biomed Mater. 2008;1(4):326-35.

59.   Stylianopoulos T, Barocas VH. Multiscale, structure-based modeling for the elastic mechanical behavior of arterial walls. J Biomech Eng. 2007;129(4):611-8.

60.   Nemat-Nasser S, Hori M. Micromechanics : overall properties of heterogeneous materials. 2nd rev. ed. Amsterdam ; New York: Elsevier; 1999. xxiv, 786 p. p.

61.   Drew DA. Averaged field equations for two-phase media. Studies in Applied Mathematics. 1971;50(2):133-66.

62.   Sander EA, Barocas VH. Comparison of 2D fiber network orientation measurement methods. J Biomed Mater Res A. 2009;88(2):322-31.

63.   Sander E, Barocas V. Biomimetic collagen tissues: collagenous tissue engineering and other applications. Collagen: Springer; 2008. p. 475-504.

64.   Stopak D, Harris AK. Connective tissue morphogenesis by fibroblast traction. I. Tissue culture observations. Dev Biol. 1982;90(2):383-98.

65.   Sawhney RK, Howard J. Slow local movements of collagen fibers by fibroblasts drive the rapid global self-organization of collagen gels. J Cell Biol. 2002;157(6):1083-91.

66.   Provenzano PP, Inman DR, Eliceiri KW, Trier SM, Keely PJ. Contact guidance mediated three-dimensional cell migration is regulated by Rho/ROCK-dependent matrix reorganization. Biophys J. 2008;95(11):5374-84.

67.   Stops AJ, McMahon LA, O'Mahoney D, Prendergast PJ, McHugh PE. A finite element prediction of strain on cells in a highly porous collagen-glycosaminoglycan scaffold. J Biomech Eng. 2008;130(6):061001.

68.   Yan KC, Nair K, Sun W. Three dimensional multi-scale modelling and analysis of cell damage in cell-encapsulated alginate constructs. Journal of biomechanics. 2010;43(6):1031-8.

69.   Sander E, Stein A, Swickrath M, Barocas V. Out of many, one: modeling schemes for biopolymer and biofibril networks. Trends in Computational Nanomechanics: Springer Netherlands; 2010. p. 557-602.

70.   Janmey PA, Euteneuer U, Traub P, Schliwa M. Viscoelastic properties of vimentin compared with other filamentous biopolymer networks. J Cell Biol. 1991;113(1):155-60.

71.   Freyman TM, Yannas IV, Yokoo R, Gibson LJ. Fibroblast contractile force is independent of the stiffness which resists the contraction. Exp Cell Res. 2002;272(2):153-62.

72.   Billiar KL, Sacks MS. Biaxial mechanical properties of the native and glutaraldehyde-treated aortic valve cusp: Part II--A structural constitutive model. J Biomech Eng. 2000;122(4):327-35.

73.   Bonet J, Wood R. Nonlinear continuum mechanics for finite element analysis. 1997. Cambridge University Press, Cambridge.

74.   Stein AM, Vader DA, Weitz DA, Sander LM. The Micromechanics of Three-Dimensional Collagen-I Gels. Complexity. 2011;16(4):22-8.

75.   Reinhardt JW, Krakauer DA, Gooch KJ. Complex Matrix Remodeling and Durotaxis Can Emerge From Simple Rules for Cell-Matrix Interaction in Agent-Based Models. Journal of biomechanical engineering. 2013;135(7):071003.

76.   Gaudet C, Marganski WA, Kim S, Brown CT, Gunderia V, Dembo M, et al. Influence of type I collagen surface density on fibroblast spreading, motility, and contractility. Biophysical journal. 2003;85(5):3329-35.

77.   Baum BJ, Zheng C, Cotrim AP, Goldsmith CM, Atkinson JC, Brahim JS, et al. Transfer of the AQP1 cDNA for the correction of radiation-induced salivary hypofunction. Biochimica et biophysica acta. 2006;1758(8):1071-7.

78.   Deshpande VS, McMeeking RM, Evans AG. A bio-chemo-mechanical model for cell contractility. Proceedings of the National Academy of Sciences of the United States of America. 2006;103(38):14015-20.

79.   Wang H, Svoronos AA, Boudou T, Sakar MS, Schell JY, Morgan JR, et al. Necking and failure of constrained 3D microtissues induced by cellular tension. Proceedings of the National Academy of Sciences of the United States of America. 2013;110(52):20923-8.

80.   Wen Q, Janmey PA. Polymer physics of the cytoskeleton. Current Opinion in Solid State and Materials Science. 2011;15(5):177-82.

81.   Munevar S, Wang Y, Dembo M. Traction force microscopy of migrating normal and H-ras transformed 3T3 fibroblasts. Biophys J. 2001;80(4):1744-57.

82.   Yang Z, Lin JS, Chen J, Wang JH. Determining substrate displacement and cell traction fields--a new approach. J Theor Biol. 2006;242(3):607-16.

83.   Yeoh OH. Some Forms of the Strain-Energy Function for Rubber. Rubber Chem Technol. 1993;66(5):754-71.

84.   Hadi MF, Sander EA, Barocas VH. Multiscale model predicts tissue-level failure from collagen fiber-level damage. J Biomech Eng. 2012;134(9):091005.

85.   Sander EA, Stylianopoulos T, Tranquillo RT, Barocas VH. Image-based multiscale modeling predicts tissue-level and network-level fiber reorganization in stretched cell-compacted collagen gels. Proc Natl Acad Sci U S A. 2009;106(42):17675-80.

86.   Mehrotra S, Hunley SC, Pawelec KM, Zhang LX, Lee I, Baek S, et al. Cell Adhesive Behavior on Thin Polyelectrolyte Multilayers: Cells Attempt to Achieve Homeostasis of Its Adhesion Energy. Langmuir : the ACS journal of surfaces and colloids. 2010;26(15):12794-802.

87.   Ma X, Schickel ME, Stevenson MD, Sarang-Sieminski AL, Gooch KJ, Ghadiali SN, et al. Fibers in the extracellular matrix enable long-range stress transmission between cells. Biophys J. 2013;104(7):1410-8.

88.   Mohammadi H, Arora PD, Simmons CA, Janmey PA, McCulloch CA. Inelastic behaviour of collagen networks in cell-matrix interactions and mechanosensation. J R Soc Interface. 2015;12(102):20141074.

89.   Wang H, Abhilash AS, Chen CS, Wells RG, Shenoy VB. Long-range force transmission in fibrous matrices enabled by tension-driven alignment of fibers. Biophys J. 2014;107(11):2592-603.

90.   Notbohm J, Lesman A, Rosakis P, Tirrell DA, Ravichandran G. Microbuckling of fibrin provides a mechanism for cell mechanosensing. Journal of the Royal Society, Interface / the Royal Society. 2015;12(108).

91.   Picu RC. Mechanics of random fiber networks-a review. Soft Matter. 2011;7(15):6768-85.

92.   Chandran PL, Barocas VH. Deterministic material-based averaging theory model of collagen gel micromechanics. Journal of biomechanical engineering. 2007;129(2):137-47.

93.   Stylianopoulos T, Barocas VH. Volume-averaging theory for the study of the mechanics of collagen networks. Comput Method Appl M. 2007;196(31-32):2981-90.

94.   Hadi MF, Sander EA, Ruberti JW, Barocas VH. Simulated remodeling of loaded collagen networks via strain-dependent enzymatic degradation and constant-rate fiber growth. Mechanics of materials : an international journal. 2012;44:72-82.

95.   Gibson LJ. Biomechanics of cellular solids. Journal of biomechanics. 2005;38(3):377-99.

APPENDIX A

Here, as in chapter 4, we directly compared the mechanical response of substrates of varying thickness subjected to a constant traction force using either the *Growth Network* or the *Delaunay Network* fiber models, but instead of the shear test, the parameters governing each model were selected so that the stress-strain response of each model matched the macroscopic uniaxial mechanical behavior of an acellular fibrin gel representative of those used as substrates for the study of cell mechanosensing.

Fibrin Gel Mechanical Characterization and Model Parameter Optimization

To determine the bulk mechanical behavior of a representative fibrin matrix used for mechanobiological studies, acellular fibrin gels were produced by mixing stock solutions of bovine fibrinogen, $CaCl_2$, and thrombin. The solution was cast into a rectangular fibrin gel and placed between low force compression grips and mounted in a BioTense Bioreactor (ADMET, Norwood, MA) equipped with a 250-gram load cell. The sample was subjected to uniaxial extension at a rate of 10 mm/min until failure, and the force and elongation data was plotted as First Piola-Kirchhoff stress (F/A_o) versus stretch ratio, λ, (l/l_o) (Figure A-1). The experiment was simulated for both *Fiber* models (described in chapter 4) using a finite element mesh that matched the geometry and boundary conditions of the experiment. Model parameters were selected until the mechanical response approximated the experimental test (Figure A-1).
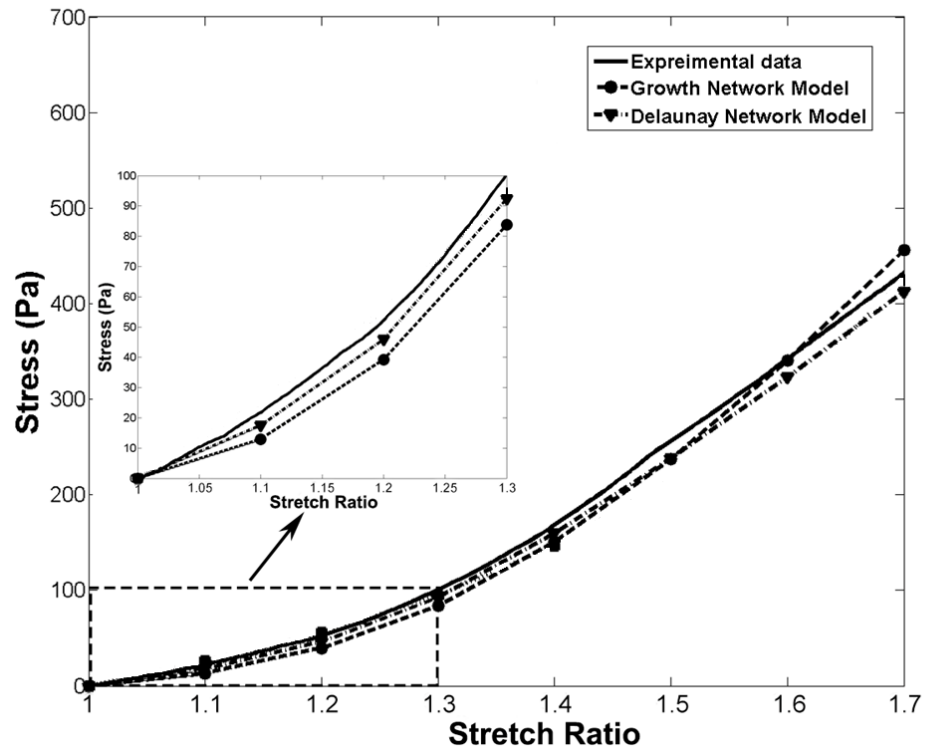
79

Figure A-1: Uniaxial extension simulations results fitted to experimental data for an acellular fibrin gel. Model parameters were selected to match the nonlinear increase in stress with stretch.

Models and Boundary Conditions

A schematic of the model is shown in Figure 4-1, and described in chapter 4. A total traction force of 0.11 nN, which is equivalent to a low traction stress of 4.60 Pa, was applied to the focal adhesion nodes by equally dividing this total force amongst the nodes and over 50 equally spaced steps.

Comparison between Growth Network and Delaunay Network Fiber Models

Material parameters were selected for each model (Table A-1) so that the simulated uniaxial stress-strain curves approximated an experimentally generated fibrin

80

gel stress-strain curve up to a stretch ratio of 1.7 (Figure A-1). The fibrin gel demonstrated a typical nonlinear strain stiffening response with increasing stretch. The material properties chosen for each model to match this nonlinear response resulted in the *Growth Network* model exhibiting slightly softer behavior compared to the experiment at low to mid-level strains (i.e., up to a Lagrangian strain of 34.5%). This region of the curve is highlighted because the maximum strains developed in the simulations for the applied traction force were less than 25%.

Table A-1: Material parameters values used for each model.

Growth Network Model:	$E_f A_f = 3 \times 10^{-10} \, \text{N}; \; B = 4; \; G = 1 \, \text{Pa}; \; v = 0.3$
Delaunay Network Model:	$E_f A_f = 1.6 \times 10^{-10} \, \text{N}; \; B = 4; \; G = 1 \, \text{Pa}; \; v = 0.3$

In order to better assess the role of fiber network microstructure in the model, we investigated differences between *Growth Network* and *Delaunay Networks*. The model parameters selected to match the experiment for the *Delaunay Network* model (Table A-1) produced a mechanical response that was slightly stiffer than the *Growth Network* model in the low stretch region (Figure A-1 inset). Even though the uniaxial mechanical response of the *Delaunay Network* model closely followed the *Growth Network* model in approximating the experimental data, the model simulations produced significantly different results in response to the applied cell traction force. The average maximum principal stresses in the focal adhesion area were higher and extended over a larger area in the *Growth Network* model (8.00 ± 4.10 Pa, 8.80 ± 4.20 Pa and 9.00 ± 4.70 Pa) (Figure A-2 A). The largest displacements in the models were also found in this area. These displacements were higher in the *Growth Network* model (1.1 ± 0.1 µm, 1.7 ± 0.1 µm,

81

and 1.9 ± 0.2 µm), and increased with increasing gel thickness (Figure A-3 A). Compared to the *Growth Network* model, both the average principal stresses (4.60 ± 3.00 Pa, 4.60 ± 300 Pa and 4.50 ± 300 Pa) and average displacements (0.33 ± 0.02 µm, 0.40 ± 0.02 µm and 0.41 ± 0.02 µm) were several-fold lower in the focal adhesion area for the *Delaunay Network* model (Figure A-2 B, Figure A-3 B) at 10 µm, 30 µm, and 50 µm, respectively.
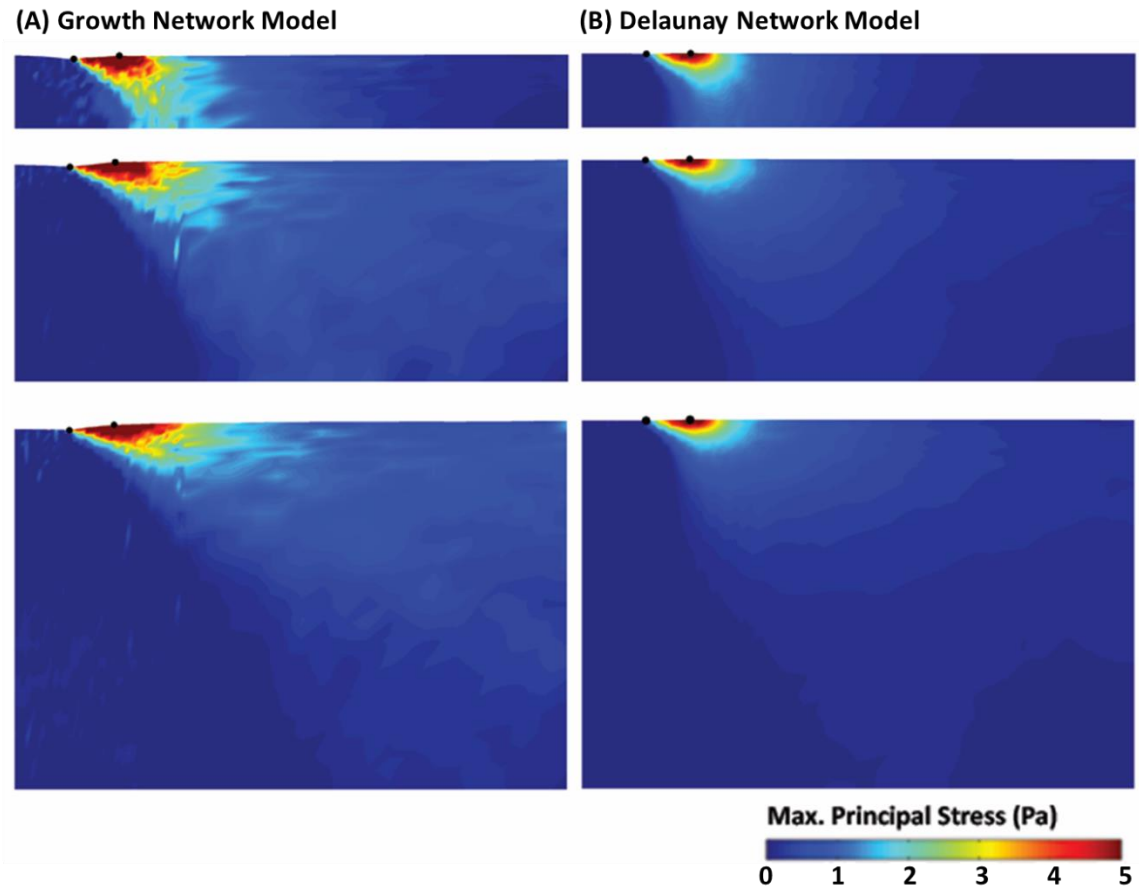

Figure A-2: Maximum principal stress for 10 µm, 30 µm, and 50 µm thick gels. Stress contours for the (A) *Growth Network* model, and the (B) *Delaunay Network* model. Black nodes correspond to the inner and outer nodes of the focal adhesion area where the cell forces were applied.

(A) Growth Network Model   **(B) Delaunay Network Model**

Displacement (microns)

0   0.1   0.2   0.3   0.4   0.5

Figure A-3: Displacement fields for 10 µm, 30 µm, and 50 µm thick gels for the (A) *Growth Network* model, and the (B) *Delaunay Network* model. Black nodes correspond to the inner and outer nodes of the focal adhesion area where the cell forces were applied.
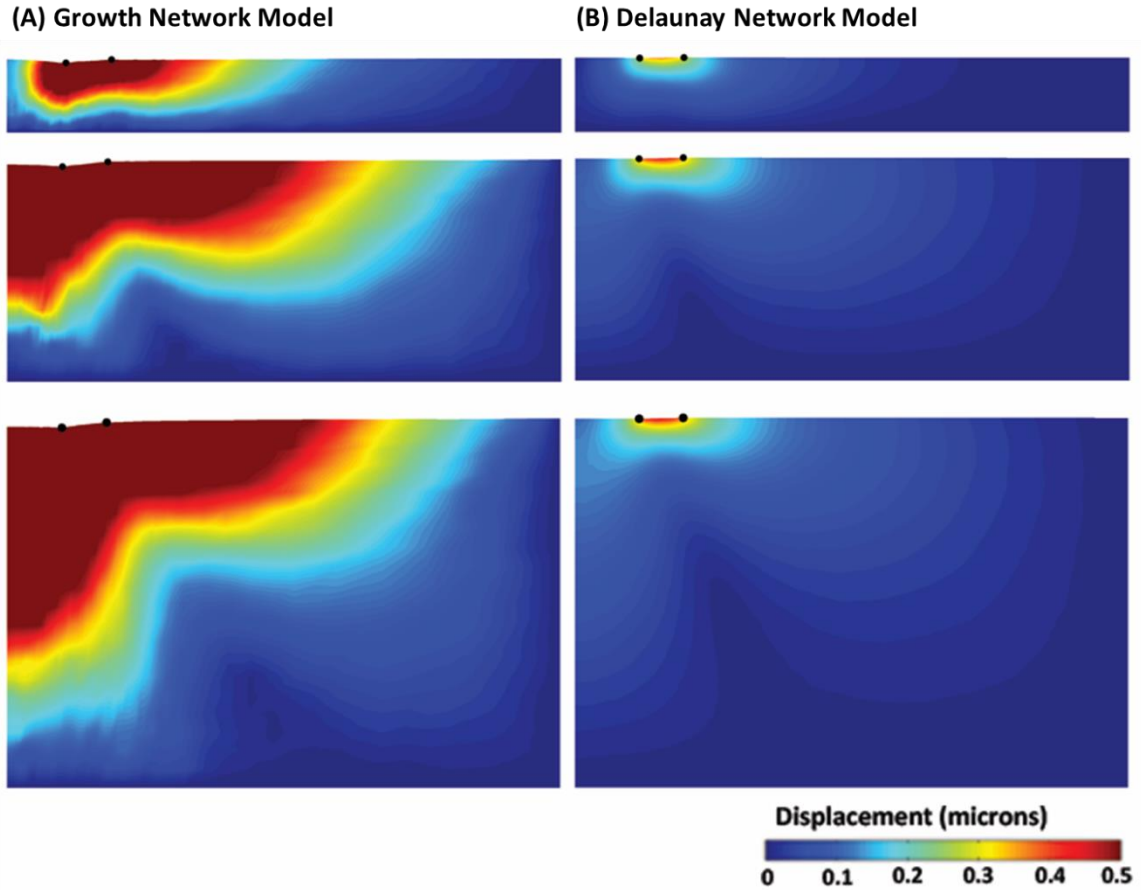
A detailed view of how two networks in the 10 µm thick *Growth Network* model reorganized in response to the cell traction force is depicted in Figure A-4. The first network (Figure A-4 A), which was located outside the focal adhesion area just underneath the inner region of the cell, gradually elongated in the vertical direction while compressing laterally and rotating slightly to the right to produce a small shearing motion. At the conclusion of the simulation (i.e., Step 50), 79% of the fibers in this network were in tension (2.2 ± 1.0 pN) and 21% of the fibers were in compression (-5.2 ± 17.5 pN). Combined, these tensile and compressive forces corresponded to an average

network fiber force of 0.7 ± 12.4 pN (maximum and minimum fiber forces of 94.4 pN and -94.7 pN, respectively). A second network (Figure A-4 B), located directly under and just inside the inner boundary of the focal adhesion area, reorganized differently. This network experience a much larger shearing motion with fibers aligning diagonally toward the direction of the applied force. At Step 50, 77% of the fibers were in tension (6.2 ± 16.2 pN) and 23% were in compression (-18.2 ± 25.9 pN), which corresponded to an average fiber force of 0.7 ± 21.4 pN (maximum and minimum fiber forces of 139.5 pN and -94.3 pN, respectively). As the gel thickness increased, the magnitudes and distribution of forces in these same networks also changed. For the 50 µm case (data not shown), the average forces at Step 50 for both networks increased roughly 57% and 286% to 1.1 ± 16.1 pN (Figure A-4 A) and 2.7 ± 23.7 pN (Figure A-4 B), respectively. In addition, the degree of anisotropy (α) for these networks also increased approximately 39% and 32%, respectively, between the 10 µm and 50 µm thick gels.
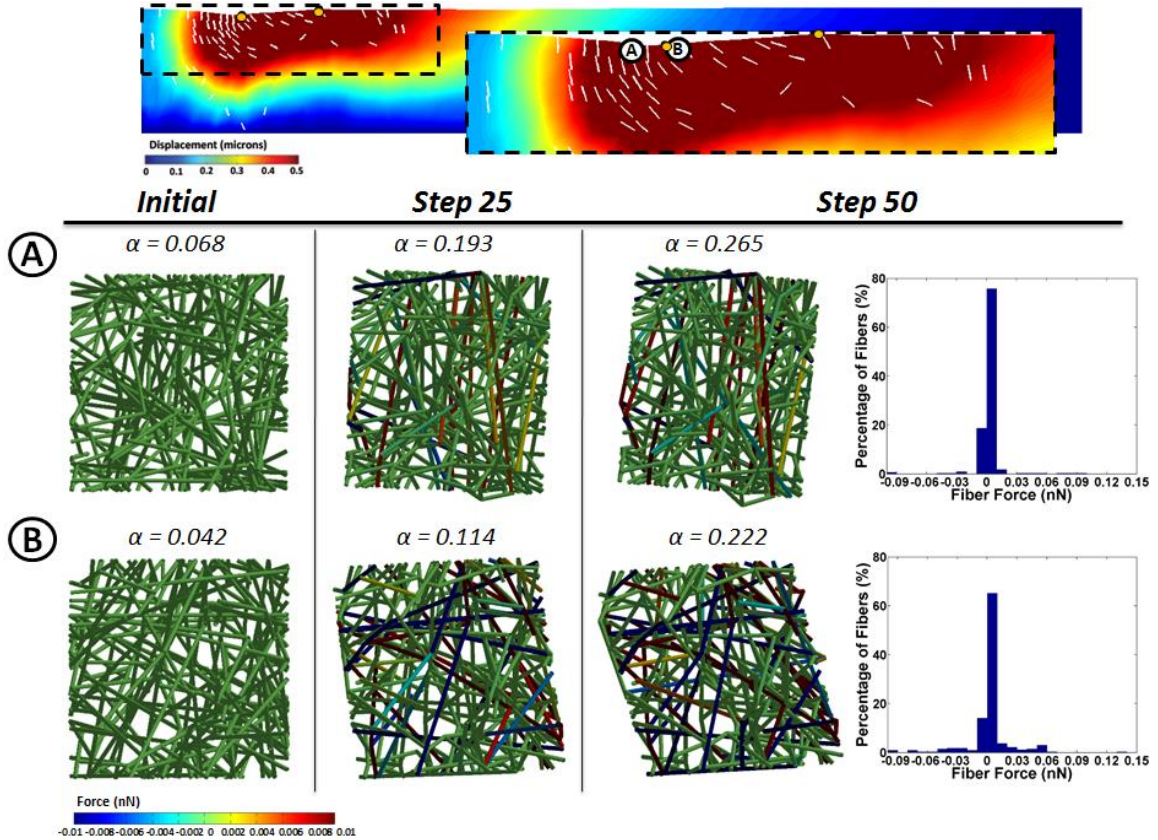
Figure A-4: *Growth* fiber network behavior at selected locations. Depicted is the 10 µm case with a sub region consisting of 320 finite elements indicated by the dashed line and enlarged. The direction of fiber alignment is shown on the displacement field for $\Delta\alpha > 0.1$, the orange circles indicate the inner and outer boundaries of the focal adhesion area, and the lettered white circles indicate the locations of networks A and B. Network organization, fiber forces, and fiber anisotropy index are shown for the initial, middle, and final steps of the simulation. Fiber force histograms are also shown for the final step of the simulation.

The number of networks with increased fiber realignment (α) and the magnitude of the change in fiber alignment with respect to the initial network configuration in the unloaded state ($\Delta\alpha$) also grew with increasing gel thickness. For example, model-wide 60, 98, and 116 finite elements had networks with a change in network fiber alignment of $\Delta\alpha > 0.1$, with average $\Delta\alpha$ values of 0.130 ± 0.026, 0.139 ± 0.035 and 0.144 ± 0.037, for gel thicknesses of 10 µm, 30 µm, and 50 µm, respectively. Similarly, if one considers a block of 320 elements common to all four meshes for a more even comparison, as

indicated in the magnified region depicted in Figure 8, the change in fiber alignment ($\Delta\alpha$) also increased 0.060 ± 0.043, 0.071 ± 0.054, and 0.075 ± 0.060, for gel thicknesses of 10 µm, 30 µm, and 50 µm, respectively. This pattern of enhanced network reorganization with increasing gel thickness seems to have occurred because the increasing distance of the rigid lower boundary from the gel surface reduced the constraints on fiber rotational freedom, which in turn facilitated the greater fiber alignment and lower effective stiffnesses observed in thicker gels.

Clear differences in *Delaunay Network* reorganization were also evident. Changes in network shape and volume were less pronounced, and a substantially higher fraction of fibers were in compression than tension. For example, 66% (Figure A-5 A) and 59% (Figure A-5 B) of the fibers in networks at equivalent locations as in the *Growth Network* model were in compression at Step 50. As a result, the average fiber forces in the network were -4.4 ± 7.7 pN and -6.1 ± 16.2 pN, respectively. An increase in gel thickness to 50 µm did not change the average fiber force in these two networks (-5.3 ± 9.4 pN and -6.8 ± 16.7 pN, respectively) nearly as much as in the *Growth Networks*. Fiber reorganization was also not as extensive in the *Delaunay Network* model as in the *Growth Network* model. None of the *Delaunay Networks* had a change in network fiber alignment greater than 0.1 (i.e., $\Delta\alpha > 0.1$). For the same block of 320 elements examined for the *Growth Network* model, the change in fiber alignments ($\Delta\alpha$) was not affected by gel thickness, with $\Delta\alpha = 0.0227 \pm 0.0202$, $\Delta\alpha = 0.0225 \pm 0.0209$, and $\Delta\alpha = 0.0227 \pm 0.0185$ for 10 µm, 30 µm, and 50 µm thick gels, respectively.
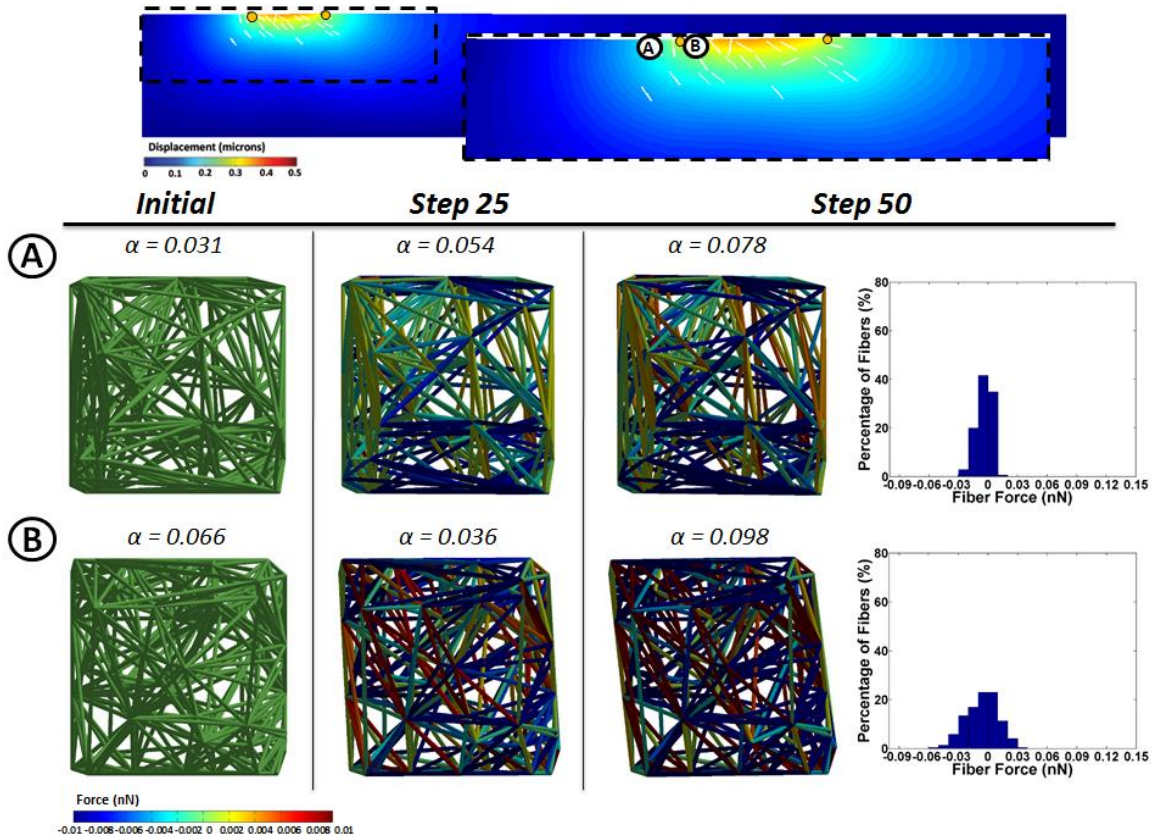
Figure A-5: *Delaunay* fiber network behavior at selected locations. Depicted is the 10 µm case with a sub region consisting of 320 finite elements indicated with the dashed line. The direction of fiber alignment is shown on the displacement field for $\Delta\alpha > 0.05$, the orange circles indicate the inner and outer boundaries of the focal adhesion area, and the lettered white circles indicate the locations of networks A and B. Network organization, fiber forces, and fiber anisotropy index are shown for the initial, middle, and final steps of the simulation. Fiber force histograms are also shown for the final step.

Aspect of the microstructure responsible for the results

Fibrous biological materials, such as collagen gels, fibrin gels, and native soft tissues, possess several mechanical characteristics that differentiate them from non-fibrous materials, including non-affine fiber deformations, strain stiffening, axial coupling under biaxial stretch, etc. These characteristics make modeling these tissues difficult because non-fibrous constitutive laws are extremely limited in their ability to replicate these behaviors. Even constitutive laws that do incorporate fibers, typically in

the form of distribution of fiber angles, are unable to account for complex fiber-fiber interactions and non-affine deformations.

It was found that the *Delaunay Network* model produced much lower stresses and displacements in response to the applied cell traction force than the *Growth Network* model, even though both models closely approximated the mechanical data obtained for a uniaxial extension test on a fibrin gel. The mechanical state of the networks in the *Growth* and *Delaunay Network* models were similar when matching the fibrin gel stretch data shown in Figure A-1. At 30% stretch, the axial component of the network volume-averaged stresses were about 80 Pa and 90 Pa, the average network fiber forces were 120 $\pm$ 210 pN and 110 $\pm$ 160 pN, and the tension:compression ratio was 90:10 and 70:30 in the *Growth* and *Delaunay Networks*, respectively, results consistent with the fact that both Fiber models produced similar stress-strain curves that matched the experimental data. The mechanical state of the networks in the *Growth Network* model in response to cell traction force was similar, but for the *Delaunay Networks* the mechanical behavior was quite different, particularly with regard to the majority of fibers being in compression.

To better understand why the *Delaunay* network behavior was different we subjected the top surface of all three 10 µm thick models to a uniformly applied 4.30 Pa shear stress and compared the mechanical response (Figure A-6).
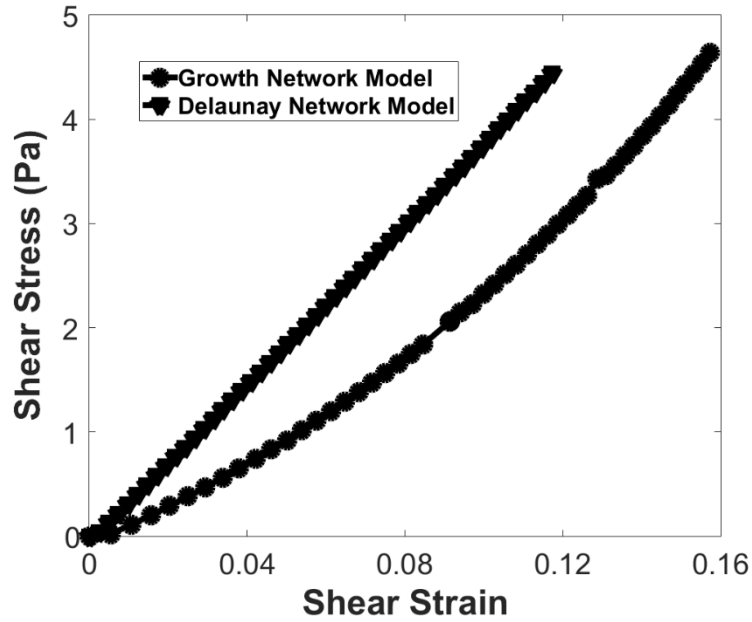
Figure A-6: Shear simulations results with the same model parameters selected to match the nonlinear increase in stress with stretch.

A closer look at how two representative fiber networks in the *Growth Network* and *Delaunay Network* models behave in response to the uniaxial extension and the shear force is shown in Figure A-7. In response to the shear, the *Growth* network, 80% and 20% of the fibers undergo tension and compression respectively with an average network fiber forces of 4 ± 12 pN; in the *Delaunay* network, 55% and 45% of the fibers are in tension and compression respectively with an average network fiber forces of 1 ± 10 pN. This indicates that although the *Growth* and *Delaunay* networks exhibit similar responses to the uniaxial extension, their responses to the shear are different. At the same amount of shear strain (10%), the shear component of the network volume-averaged stress tensor, are about 2.00 Pa and 4.00 Pa in the *Growth* and *Delaunay* networks respectively, and demonstrate that during the application of shear force the *Delaunay* network exhibits a stiffer behavior than the *Growth* network. Thus, the displacements are much less in the

89

Delaunay Network model than in the *Growth Network* model in response to the applied
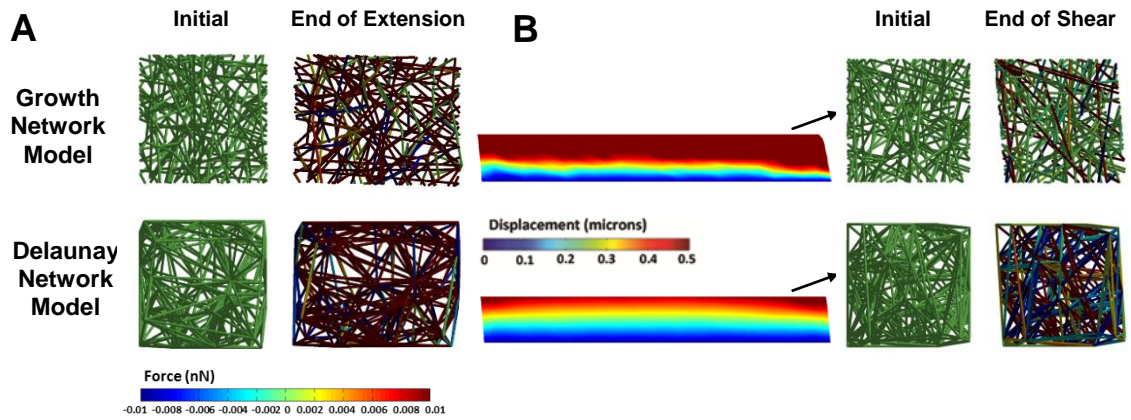
shear force.

Figure A-7: Behavior of selected *Growth* and *Delaunay* fiber networks in response to (A) uniaxial extension, and (B) shear test.

APPENDIX B

Force balance equations

x-coordinate of node *i*:

$$\mu_{0i}\frac{\partial x_i}{\partial t} + \sum_{j=1}^{M_i}\left(\mu\frac{\partial \varepsilon_{ij}}{\partial t} + E_{ij}\varepsilon_{ij}\right)cos\varphi_{ij} = \left|F_i^{Active}\right|cos\alpha_i$$

y-coordinate of node *i*:

$$\mu_{0i}\frac{\partial y_i}{\partial t} + \sum_{j=1}^{M_i}\left(\mu\frac{\partial \varepsilon_{ij}}{\partial t} + E_{ij}\varepsilon_{ij}\right)sin\varphi_{ij} = \left|F_i^{Active}\right|sin\alpha_i$$

Discretization for x-coordinate:

$$\mu_{0i}\frac{x\_new_i - x_i}{\Delta t} + \sum_{j=1}^{M_i}\left(\mu\frac{\varepsilon\_new_{ij} - \varepsilon_{ij}}{\Delta t} + E_{ij}\varepsilon_{ij}\right)cos\varphi_{ij} = \left|F_i^{Active}\right|cos\alpha_i$$

$$x\_new_i^{p+1} = x_i + \frac{\left(-\sum_{j=1}^{M_i}(E_{ij}\varepsilon_{ij})cos\varphi_{ij} + \left|F_i^{Active}\right|cos\alpha_i\right)\Delta t - \sum_{j=1}^{M_i}\mu\left(\varepsilon\_new_{ij}^{p} - \varepsilon_{ij}\right)cos\varphi_{ij}}{\mu_{0i}}$$

Similar for *y*-coordinate…

91